Onset of thermal convection in a rectangular parallelepiped cavity of small aspect ratios

Funakoshi, Mitsuaki

Onset of Thermal Convection in a Rectangular Parallelepiped Cavity of Small Aspect Ratios

Mitsuaki Funakoshi

Professor Emeritus, Kyoto University, Yoshida-Honmachi, Sakyo-ku, Kyoto 606-8501, Japan

E-mail: `funakoshi.mitsuaki.56m@st.kyoto-u.ac.jp`

Abstract. Onset of thermal convection of a fluid in a rectangular parallelepiped cavity of small aspect ratios is examined both numerically and analytically under the assumption that its all walls are rigid and of perfect thermal conductance exposed to a vertically linear temperature field. Critical Rayleigh number R_c and the steady velocity and temperature fields of most unstable modes are computed by a Galerkin spectral method of high accuracy for aspect ratios A_x and A_y either or both of which are small.

We find that if A_x is decreased to 0 with A_y being kept constant, R_c increases proportionally to A_x^{-4}, the convection rolls of most unstable mode whose axes are parallel to the shorter side walls become narrower, and their number increases proportionally to $A_x^{-\frac{1}{2}}$. Moreover, as A_x is decreased, we observe the changes of the symmetry of most unstable mode that occur more frequently for smaller A_x. However, if $A_x = A_y = A$ is decreased to 0, although we again observe the increase in R_c proportional to A^{-4}, we obtain only one narrow convection roll as the velocity field of most unstable mode for all A.

The expressions of R_c and velocity fields in the limit of $A_x \to 0$ or $A \to 0$ are obtained by an asymptotic analysis in which the dependences of R_c and the magnitude and length scale of velocity fields of most unstable modes on A_x and A_y in the numerical computations are used. For example, R_c is approximated by $\pi^4 A_x^{-4}$ and $25\pi^4 A^{-4}$ in the limits of $A_x \to 0$ and $A \to 0$, respectively. Moreover, analytical expressions of some components of velocity fields in these limits are derived. Finally, we find that for small A_x or A the agreement between the numerical and analytical results on R_c and velocity field is quite good except for the velocity field in thin wall layers near the top and bottom walls.

1. Introduction

Because the onset of thermal convection of a fluid in a closed cavity is an interesting problem in fluid dynamics and also important in applications, it has been investigated theoretically, numerically or experimentally in several studies for many years (see, for example, Gershuni and Zhukhovitskii (1972), Koschmieder (1993), Lappa (2010), and references therein.). Some of these studies examined the onset of three-dimensional thermal convection in a rectangular parallelepiped cavity of rigid walls for several values of aspect ratios $A_x = L_x/d$ and $A_y = L_y/d$, where L_x and L_y are horizontal lengths of the cavity, and d is its height. Koschmieder (1966) experimentally investigated this problem and showed that if both A_x and A_y are larger than 1 and the difference between them is not small, the pattern of flows that appears first as the difference in temperatures on upper and lower walls is increased slowly is a linear arrangement of several convection rolls of nearly square cross-section whose axes are horizontal and parallel to shorter side walls. Stork and Müller (1972) also obtained similar results for A_x and A_y larger than 1 in their experiments on the onset of three-dimensional thermal convection in a rectangular parallelepiped cavity with side walls where an essentially linear vertical temperature profile is maintained. Moreover, they pointed out that if one of the aspect ratios is smaller than 1, the widths of observed convection rolls whose axes are parallel to the shorter side walls are smaller than their height. For example, in the experiments with A_y between 3 and 6, they found that the number of observed convection rolls is larger than A_y if A_x is 0.7 or 0.5, although detailed examination of convection rolls for A_x less than 0.5 was not performed. They also observed the tendency that R_c increases rapidly as A_x decreases from 1 with A_y being kept constant.

Davis (1967) numerically examined the onset of thermal convection in a rectangular parallelepiped cavity with walls of perfect thermal conductance. If the temperatures on upper and lower walls are constants, and the temperature on side walls is a linear function of vertical coordinate connecting these temperatures, the motionless state (thermal conduction state) of a fluid in the cavity is possible. He examined the critical Rayleigh number R_c of this state and the flow pattern of most unstable mode that is destabilized at this Rayleigh number for several values of aspect ratios A_x and A_y. In this examination, he adopted the assumption of finite roll, in which a horizontal component of fluid velocity normal to a side wall is 0, and obtained the results that R_c rapidly increases with the decrease in one of A_x and A_y and that the change of most unstable modes frequently occurs with their decrease to 0. Moreover, he found that if both A_x and A_y are larger than 1 and the difference between them is not small, the flow patterns of most unstable mode are similar to those observed in the experiments mentioned above at the onset of thermal convection. When either A_x or A_y is smaller than 1, he obtained the flow patterns of most unstable mode composed of a few narrow convection rolls for which their height is larger than their width, which is consistent with the experimental observation by Stork and Müller (1972). Although Davis (1967) obtained the above remarkable and interesting results, his study is not perfect because the assumption of finite roll cannot be satisfied exactly by the solutions to governing equations of thermal convection, as was pointed out by Davies-Jones (1970).

After the study by Davis (1967), there were several numerical studies aiming at the determination of R_c and/or most unstable modes for many values of aspect ratios of a three-dimensional rectangular or cubic cavity with rigid walls of perfect thermal conductance (see, for example, Catton (1970), Gershuni and Zhukhovitskii (1972) and Kirchartz and Oertel (1988)). The computation of R_c and most unstable modes with high accuracy was carried out by Mizushima and Matsuda (1996, 1997) for cubic and rectangular parallelepiped cavities. Fukazawa and Funakoshi (2015) systematically examined R_c and the flow patterns of most unstable mode for several values of A_x and A_y using a Galerkin spectral method of high accuracy. They found the tendency that R_c increases rapidly as either A_x or A_y decreases to 0, and decreases slowly as both A_x and A_y increase. They examined the flow pattern of most unstable mode in detail for $1 \leq A_x, A_y \leq 6$, and showed that the flow pattern is a linear arrangement of several convection rolls of nearly square cross-section whose axes are horizontal and parallel to shorter side walls if the difference between A_x and A_y is not small. They also observed frequent change of most unstable mode and rapid increase in R_c with the decrease in either A_x or A_y from 1.

The onset of thermal convection in a three-dimensional rectangular or cubic cavity for different boundary conditions was also examined numerically in several studies. For example, Edwards (1988) obtained R_c and the flow patterns of most unstable mode for A_x and A_y between 1 and 12 under the assumption of adiabatic side walls. Mizushima and Nakamura (2003) also examined the dependence of R_c and the flow patterns on A_x and A_y that are 1 or more for the same thermal boundary condition on side walls. The Bénard-Marangoni instability in a rectangular parallelepiped cavity for A_x and A_y between 1 and 9 was examined by Dauby and Lebon (1996) for adiabatic side walls and a convective cooling condition on the top wall. Gelfgat (1999) examined the R_c and symmetries of most unstable modes for A_x and A_y larger than 1 for adiabatic side walls and stress-free and convective cooling conditions on the top wall. Moreover, there are several numerical studies on the bifurcations of steady solutions of nonlinear governing equations of thermal convection in three-dimensional cubic or rectangular cavities for different boundary conditions on the walls (for example, see Puigjaner et al. (2006, 2008), Lappa (2010), and references therein). However, the case of small aspect ratios was not examined in the above linear stability analysis and bifurcation analysis.

There are also numerical and analytical studies on R_c and the flow pattern of most unstable mode of thermal convection in an infinite channel of rectangular cross-section. Chana and Daniels (1989) examined this problem for rigid or stress-free boundary condition on the top and bottom walls under the assumptions of rigid side walls, no volume flux down the channel, and perfect thermal conductance on all the walls. For rigid top and bottom walls, they numerically calculated R_c and critical wavenumber k_c (non-dimensionalized with d) for several values of aspect ratio $A_x = L_x/d$ of cross-section, where L_x and d are horizontal and vertical length of the cross-section, respectively. They found that R_c rapidly increases as A_x decreases from 1 and that for sufficiently small A_x, k_c increases as A_x decreases. They also examined the characteristics of velocity and temperature fields of most unstable mode mainly for $A_x \geq 1$. Moreover, they performed an asymptotic analysis in which the asymptotic forms of R_c, k_c, and velocity and temperature fields of most unstable mode in the limits of $A_x \to 0$ and $A_x \to \infty$ were obtained. Daniels and Ong (1990) also numerically computed the values of R_c and k_c with higher accuracy than Chana and Daniels (1989) for a few A_x's between 1/2 and 4, and compared these values with the above asymptotic forms of R_c and k_c.

In the preceding numerical studies introduced above, the dependence of R_c and the velocity field of most unstable mode on aspect ratios A_x and A_y of a rectangular parallelepiped cavity was not examined in detail when either or both of A_x and A_y are smaller than 1. However, the rapid increase in R_c and the increase in the number of convection rolls of most unstable mode and their narrowing with the decrease in either A_x or A_y from 1 are interesting behavior. Therefore, in the present study, we first aim at making this behavior clearer by the detailed examination of R_c and the velocity field of most unstable mode for such A_x and A_y using a numerical analysis of high accuracy and an asymptotic analysis. Moreover, since the rapid increase in R_c with the decrease in $A_x = A_y = A$ from 1 and the formation of one tall vortex roll for small A are also interesting, we also aim at describing these behaviors quantitatively by using the same numerical and analytical methods.

After the description of formulation of the considered problem in section 2, section 3 is devoted to the introduction of the numerical method used to examine the linear stability of the motionless state. The convergence of numerical solutions is shown in section 4. Numerical results on R_c and the velocity field of most unstable mode are shown in section 5. In section 6, using the dependences of R_c and the velocity and temperature fields of most unstable modes on A_x and A_y in the numerical computations, the asymptotic forms of these fields and R_c in the limits of $A_x \to 0$ and $A \to 0$ are obtained by an asymptotic analysis, and are compared with the numerical results shown in section 5. Finally, section 7 is devoted to discussion and conclusions.

2. Formulation

We consider the onset of thermal convection of an incompressible viscous fluid in a rectangular parallelepiped cavity exposed to a vertically linear temperature field. Cartesian coordinates (x^*, y^*, z^*) are defined in which x^* and y^* axes are horizontal and parallel to the side walls of the cavity, z^* axis is vertically upward, and the origin is at the center of the cavity. Two aspect ratios of the cavity are defined as $A_x \equiv L_x/d$ and $A_y \equiv L_y/d$, where L_x, L_y and d respectively denote the length of the cavity in the x^*, y^* and z^* directions. We assume that external temperature field T^*_{ex} is expressed as

$$T^*_{\mathrm{ex}}(z^*) = -\beta z^* + T^*_0, \tag{1}$$

where $\beta(>0)$ is the gradient of the external temperature, and T_0^* is the external temperature at $z^*=0$. All the walls of cavity are assumed to be rigid and of perfect thermal conductance.

Under the Boussinesq approximation, non-dimensionalized forms of the equation of continuity, Navier-Stokes equation and energy equation are written as

$$\nabla\cdot\boldsymbol{v}=0, \tag{2}$$

$$\frac{1}{P}\Big(\frac{\partial}{\partial t}+\boldsymbol{v}\cdot\nabla\Big)\boldsymbol{v}=-\nabla p+\Delta\boldsymbol{v}-\Big\{\frac{gd^3}{\kappa\nu}-R(T-T_0)\Big\}\boldsymbol{e}_z, \tag{3}$$

$$\Big(\frac{\partial}{\partial t}+\boldsymbol{v}\cdot\nabla\Big)T=\Delta T, \tag{4}$$

where

$$\nabla\equiv\boldsymbol{e}_x\frac{\partial}{\partial x}+\boldsymbol{e}_y\frac{\partial}{\partial y}+\boldsymbol{e}_z\frac{\partial}{\partial z},\quad \Delta\equiv\frac{\partial^2}{\partial x^2}+\frac{\partial^2}{\partial y^2}+\frac{\partial^2}{\partial z^2},$$

and velocity $\boldsymbol{v}^*$, temperature T^*, pressure p^* of fluid, spatial coordinates (x^*,y^*,z^*), and the time t^* are non-dimensionalized as

$$x\equiv\frac{x^*}{d},\ y\equiv\frac{y^*}{d},\ z\equiv\frac{z^*}{d},\ t\equiv\frac{\kappa}{d^2}t^*,\ \boldsymbol{v}\equiv\frac{d}{\kappa}\boldsymbol{v}^*,\ T\equiv\frac{T^*}{\beta d},\ p\equiv\frac{d^2}{\rho_0\kappa\nu}p^*. \tag{5}$$

Moreover, $\boldsymbol{e}_x$, $\boldsymbol{e}_y$ and $\boldsymbol{e}_z$ respectively represent the unit vectors in the x^*, y^* and z^* directions, and ρ_0 is the density of fluid for $T^*=T_0^*$. Also ν, α and κ respectively denote the kinematic viscosity, the coefficient of thermal expansion, and the thermal diffusivity of fluid, g is the acceleration due to gravity, and $T_0\equiv T_0^*/(\beta d)$. Two non-dimensional parameters R and P in equation (3) respectively denote the Rayleigh number and the Prandtl number defined by

$$R\equiv\frac{\alpha g\beta d^4}{\kappa\nu},\qquad P\equiv\frac{\nu}{\kappa}.$$

Non-dimensionalized boundary conditions for the velocity and temperature on the walls of the cavity are expressed as

$$\boldsymbol{v}=0,\ T=T_{\rm ex}(z)\quad \text{on}\ x=\pm\frac{A_x}{2},\ \text{on}\ y=\pm\frac{A_y}{2},\ \text{and on}\ z=\pm\frac{1}{2}, \tag{6}$$

where

$$T_{\rm ex}(z)=-z+T_0. \tag{7}$$

If we define the deviations of velocity, temperature and pressure from those in the motionless state as

$$\boldsymbol{u}\equiv\boldsymbol{v}-\boldsymbol{v}_s,\ \ \theta\equiv T-T_s,\ \ q\equiv p-p_s, \tag{8}$$

we obtain the following governing equations:

$$\nabla\cdot\boldsymbol{u}=0, \tag{9}$$

$$\frac{1}{P}\Big(\frac{\partial}{\partial t}+\boldsymbol{u}\cdot\nabla\Big)\boldsymbol{u}=-\nabla q+\Delta\boldsymbol{u}+R\theta\boldsymbol{e}_z, \tag{10}$$

$$\left(\frac{\partial}{\partial t}+\boldsymbol{u}\cdot\nabla\right)\theta=\Delta\theta+\boldsymbol{u}\cdot\boldsymbol{e}_z, \tag{11}$$

where

$$\boldsymbol{v}_s=0,\ \ T_s=T_{\rm ex}(z),\ \ p_s=-\frac{1}{2}Rz^2-\frac{gd^3}{\kappa\nu}z+p_0, \tag{12}$$

and p_0 is the pressure at $z=0$. Boundary conditions for $\boldsymbol{u}$ and θ are written as

$$\boldsymbol{u}=0,\ \theta=0 \quad \text{on}\ \ x=\pm\frac{A_x}{2},\ \ \text{on}\ \ y=\pm\frac{A_y}{2},\ \ \text{and on}\ \ z=\pm\frac{1}{2}, \tag{13}$$

3. Stability analysis of motionless state

We examine the linear stability of the motionless state on the basis of linearized version of equations (9)–(11) and boundary condition (13). The variables $\boldsymbol{u}$, θ and q in these equations are assumed to be of the following time dependences:

$$\boldsymbol{u}=e^{\lambda t}\hat{\boldsymbol{u}}+\text{c.c.},\ \ \theta=e^{\lambda t}\hat{\theta}+\text{c.c.},\ \ q=e^{\lambda t}\hat{q}+\text{c.c.}, \tag{14}$$

where $\hat{\boldsymbol{u}}$, $\hat{\theta}$ and $\hat{q}$ are complex-valued functions of x, y and z. Also λ is a complex constant, and c.c. denotes the complex conjugate of preceding terms. Critical Rayleigh number R_c is defined as the value of R for which the motionless state is neutrally stable, that is, the real part of λ equals to 0. Sherman and Ostrach (1966) showed that λ is always real for positive R if the linearized version of equations (9)–(11) and boundary condition (13) are satisfied. Therefore, the value of R_c is obtained under the condition of $\lambda=0$.

Governing equations for $\hat{\boldsymbol{u}}$, $\hat{\theta}$ and $\hat{q}$ of neutrally stable disturbances are expressed as

$$\nabla\cdot\hat{\boldsymbol{u}}=0, \tag{15}$$

$$-\nabla\hat{q}+\Delta\hat{\boldsymbol{u}}+R_c\hat{\theta}\boldsymbol{e}_z=0, \tag{16}$$

$$\Delta\hat{\theta}+\hat{\boldsymbol{u}}\cdot\boldsymbol{e}_z=0. \tag{17}$$

Here $\hat{\boldsymbol{u}}, \hat{\theta}$ and $\hat{q}$ can be assumed to be real functions. The boundary conditions for $\hat{\boldsymbol{u}}$ and $\hat{\theta}$ are written as

$$\hat{\boldsymbol{u}}=0,\ \hat{\theta}=0 \quad \text{on}\ \ x=\pm\frac{A_x}{2},\ \ \text{on}\ \ y=\pm\frac{A_y}{2},\ \ \text{and on}\ \ z=\pm\frac{1}{2}. \tag{18}$$

We use a Galerkin spectral method to solve numerically equations (15)–(17) under boundary condition (18). Since this method is the same as the one used in Fukazawa and Funakoshi (2015), only its main part is described here. We expand $\hat{\boldsymbol{u}}$ and $\hat{\theta}$ as

$$\hat{\boldsymbol{u}}(x,y,z)=\sum_{\ell=0}^{2L+1}\sum_{m=0}^{2M+1}\sum_{n=0}^{2N+1}\sum_{J=1}^{3}a^{(J)}_{(\ell,m,n)}\boldsymbol{f}^{(J)}_{(\ell,m,n)}(x,y,z), \tag{19}$$

$$\hat{\theta}(x,y,z)=\sum_{\ell=0}^{2L+1}\sum_{m=0}^{2M+1}\sum_{n=0}^{2N+1}b_{(\ell,m,n)}f_{(\ell,m,n)}(x,y,z), \tag{20}$$

where basis functions $\boldsymbol{f}^{(J)}_{(\ell,m,n)}(x,y,z)$ and $f_{(\ell,m,n)}(x,y,z)$ are defined by

$$\begin{cases} \boldsymbol{f}^{(1)}_{(\ell,m,n)}(x,y,z) \equiv \nabla\times F_\ell\Big(\dfrac{2}{A_x}x\Big)G_m\Big(\dfrac{2}{A_y}y\Big)G_n(2z)\boldsymbol{e}_x, \\ \boldsymbol{f}^{(2)}_{(\ell,m,n)}(x,y,z) \equiv \nabla\times G_\ell\Big(\dfrac{2}{A_x}x\Big)F_m\Big(\dfrac{2}{A_y}y\Big)G_n(2z)\boldsymbol{e}_y, \\ \boldsymbol{f}^{(3)}_{(\ell,m,n)}(x,y,z) \equiv \nabla\times G_\ell\Big(\dfrac{2}{A_x}x\Big)G_m\Big(\dfrac{2}{A_y}y\Big)F_n(2z)\boldsymbol{e}_z, \\ f_{(\ell,m,n)}(x,y,z) \equiv F_\ell\Big(\dfrac{2}{A_x}x\Big)F_m\Big(\dfrac{2}{A_y}y\Big)F_n(2z). \end{cases} \tag{21}$$

Therefore, equation (15) is satisfied for any values of expansion coefficients $a^{(J)}_{(\ell,m,n)}$. In the expression of $\hat{\boldsymbol{u}}$ given by equations (19) and (21), we use three (rather than two) vector potentials so that we can impose decoupled boundary conditions for them on all the walls of the cavity without a loss of generality. In the above basis functions, modified Chebyshev polynomials $F_\ell(\xi)$ and $G_\ell(\xi)$ defined by

$$F_\ell(\xi)\equiv(1-\xi^2)T_\ell(\xi),\;\; G_\ell(\xi)\equiv(1-\xi^2)^2T_\ell(\xi),\;\; (\ell=0,1,2,\ldots),$$

are used, where $T_\ell(\xi)$ is the Chebyshev polynomial of the ℓ-th order, and $\xi = 2x/A_x$, $2y/A_y$ or $2z$. Therefore, boundary condition (18) is satisfied for any values of expansion coefficients $a^{(J)}_{(\ell,m,n)}$ and $b_{(\ell,m,n)}$. Expansions of $\hat{\boldsymbol{u}}$ and $\hat{\theta}$ are truncated at $\ell = 2L+1, m = 2M+1$ and $n = 2N+1$ in the x, y and z directions, respectively.

Here, we introduce functions $\tilde{\boldsymbol{f}}^{(I)}_{(i,j,k)}(I=1,2,3)$ and $\tilde{f}_{(i,j,k)}$ for $i=0,1,\ldots,2L+1$, $j=0,1,\ldots,2M+1$ and $k=0,1,\ldots,2N+1$ defined by

$$\tilde{\boldsymbol{f}}^{(I)}_{(i,j,k)}(x,y,z) \equiv \begin{cases} \nabla\times\tilde{F}_i\Big(\dfrac{2}{A_x}x\Big)\tilde{G}_j\Big(\dfrac{2}{A_y}y\Big)\tilde{G}_k(2z)\boldsymbol{e}_x & (\text{for } \; I=1), \\ \nabla\times\tilde{G}_i\Big(\dfrac{2}{A_x}x\Big)\tilde{F}_j\Big(\dfrac{2}{A_y}y\Big)\tilde{G}_k(2z)\boldsymbol{e}_y & (\text{for } \; I=2), \\ \nabla\times\tilde{G}_i\Big(\dfrac{2}{A_x}x\Big)\tilde{G}_j\Big(\dfrac{2}{A_y}y\Big)\tilde{F}_k(2z)\boldsymbol{e}_z & (\text{for } \; I=3), \end{cases} \tag{22}$$

$$\tilde{f}_{(i,j,k)}(x,y,z) \equiv \tilde{F}_i\Big(\frac{2}{A_x}x\Big)\tilde{F}_j\Big(\frac{2}{A_y}y\Big)\tilde{F}_k(2z), \tag{23}$$

where functions $\tilde{F}_i(\xi)$ and $\tilde{G}_i(\xi)$ are defined as

$$\tilde{F}_i(\xi)\equiv\frac{F_i(\xi)}{\sqrt{1-\xi^2}},\qquad \tilde{G}_i(\xi)\equiv\frac{G_i(\xi)}{\sqrt{1-\xi^2}},\quad (i=0,1,2,\ldots),$$

for $\xi = 2x/A_x$, $2y/A_y$ or $2z$. To obtain linear algebraic equations for expansion coefficients $a^{(J)}_{(\ell,m,n)}$ and $b_{(\ell,m,n)}$, we impose the following conditions:

$$\langle\langle\tilde{\boldsymbol{f}}^{(I)}_{(i,j,k)}, -\nabla\hat{q}+\Delta\hat{\boldsymbol{u}}+R_c\hat{\theta}\boldsymbol{e}_z\rangle\rangle=0 \quad (\text{for } \; I=1,2,3,\; i=0,1,\ldots,2L+1, \; j=0,1,\ldots,2M+1 \text{ and } k=0,1,\ldots,2N+1), \tag{24}$$

$$\langle\tilde{f}_{(i,j,k)}, \Delta\hat{\theta}+\hat{\boldsymbol{u}}\cdot\boldsymbol{e}_z\rangle=0 \quad (\text{for } \; i=0,1,\ldots,2L+1, \; j=0,1,\ldots,2M+1 \text{ and } k=0,1,\ldots,2N+1), \tag{25}$$

where the inner product $\langle\langle \boldsymbol{f}, \boldsymbol{g} \rangle\rangle$ of vector-valued functions $\boldsymbol{f}(x, y, z)$ and $\boldsymbol{g}(x, y, z)$ is defined by

$$\langle\langle \boldsymbol{f}, \boldsymbol{g} \rangle\rangle \equiv \int_{-\frac{A_x}{2}}^{\frac{A_x}{2}} \mathrm{d}x \int_{-\frac{A_y}{2}}^{\frac{A_y}{2}} \mathrm{d}y \int_{-\frac{1}{2}}^{\frac{1}{2}} \mathrm{d}z \boldsymbol{f}(x, y, z) \cdot \boldsymbol{g}(x, y, z), \tag{26}$$

and the inner product $\langle f, g \rangle$ of scalar functions $f(x, y, z)$ and $g(x, y, z)$ is defined by

$$\langle f, g \rangle \equiv \int_{-\frac{A_x}{2}}^{\frac{A_x}{2}} \mathrm{d}x \int_{-\frac{A_y}{2}}^{\frac{A_y}{2}} \mathrm{d}y \int_{-\frac{1}{2}}^{\frac{1}{2}} \mathrm{d}z f(x, y, z) g(x, y, z). \tag{27}$$

The inner product of $\tilde{\boldsymbol{f}}^{(I)}_{(i,j,k)}$ and the term of pressure gradient in equation (24) vanishes for all I, i, j and k, because $\tilde{\boldsymbol{f}}^{(I)}_{(i,j,k)}$ satisfies conditions $\tilde{\boldsymbol{f}}^{(I)}_{(i,j,k)} = 0$ (on the walls) and $\nabla \cdot \tilde{\boldsymbol{f}}^{(I)}_{(i,j,k)} = 0$ (in the cavity).

Equations (24) and (25) are reduced to a generalized eigenvalue problem expressed as

$$A\boldsymbol{x} = \sqrt{R_c} B\boldsymbol{x}, \tag{28}$$

where eigenvector $\boldsymbol{x}$ has $N_t \equiv 4(2L + 2)(2M + 2)(2N + 2)$ components, and A and B are square matrices of dimension N_t. The $(J - 1)(2L + 2)(2M + 2)(2N + 2) + \ell(2M + 2)(2N + 2) + m(2N + 2) + n + 1$ -th component of eigenvector $\boldsymbol{x}$ expressed as $x_{(J,\ell,m,n)}$ is given by

$$x_{(J,\ell,m,n)} = \begin{cases} a^{(J)}_{(\ell,m,n)} & (J = 1, 2, 3), \\ \sqrt{R_c} b_{(\ell,m,n)} & (J = 4), \end{cases} \tag{29}$$

for $\ell = 0, 1, \ldots, 2L+1$, $m = 0, 1, \ldots, 2M+1$ and $n = 0, 1, \ldots, 2N+1$. The components of matrices A and B in the $(I-1)(2L+2)(2M+2)(2N+2)+i(2M+2)(2N+2)+j(2N+2)+k+1$ -th row and $(J-1)(2L+2)(2M+2)(2N+2)+\ell(2M+2)(2N+2)+m(2N+2)+n+1$ -th column, expressed as $a_{(I,i,j,k),(J,\ell,m,n)}$ and $b_{(I,i,j,k),(J,\ell,m,n)}$ for A and B respectively, are written as

$$a_{(I,i,j,k),(J,\ell,m,n)} = \begin{cases} \left\langle\left\langle \tilde{\boldsymbol{f}}^{(I)}_{(i,j,k)}, \Delta \boldsymbol{f}^{(J)}_{(\ell,m,n)} \right\rangle\right\rangle & (\text{for } I = 1, 2, 3,\ J = 1, 2, 3), \\ \left\langle \tilde{f}_{(i,j,k)}, \Delta f_{(\ell,m,n)} \right\rangle & (\text{for } I = J = 4), \\ 0 & (\text{otherwise}), \end{cases} \tag{30}$$

$$b_{(I,i,j,k),(J,\ell,m,n)} = \begin{cases} -\left\langle\left\langle \tilde{\boldsymbol{f}}^{(I)}_{(i,j,k)}, f_{(\ell,m,n)} \boldsymbol{e}_z \right\rangle\right\rangle & (\text{for } I = 1, 2, 3,\ J = 4), \\ -\left\langle \tilde{f}_{(i,j,k)}, \boldsymbol{f}^{(J)}_{(\ell,m,n)} \cdot \boldsymbol{e}_z \right\rangle & (\text{for } I = 4,\ J = 1, 2, 3), \\ 0 & (\text{otherwise}), \end{cases} \tag{31}$$

for $i = 0, 1, \ldots, 2L + 1$, $j = 0, 1, \ldots, 2M + 1$, $k = 0, 1, \ldots, 2N + 1$, and $\ell = 0, 1, \ldots, 2L + 1$, $m = 0, 1, \ldots, 2M + 1$, $n = 0, 1, \ldots, 2N + 1$.

There are eight symmetry modes that are defined by the reflections with respect to three planes $x = 0$, $y = 0$ and $z = 0$. These modes are expressed as $\hat{\theta}(s_x, s_y, s_z)$

mode, where s_x (or s_y, s_z) $= e$ $[o]$ means that $\hat{\theta}$ is an even [odd] function of x (or y, z). Therefore, for example in $\hat{\theta}(o, o, e)$ mode, $\hat{\theta}$ is an odd function of x and y, and also an even function of z. In $\hat{\theta}(s_x, s_y, s_z)$ mode, the symmetries of x, y and z components of $\hat{\boldsymbol{u}}$ are given by $(\bar{s}_x, s_y, \bar{s}_z)$, $(s_x, \bar{s}_y, \bar{s}_z)$ and (s_x, s_y, s_z), respectively, where $\bar{s}_x$ (or $\bar{s}_y$, $\bar{s}_z$) $= o$ $[e]$ if s_x (or s_y, s_z) $= e$ $[o]$.

Because of the symmetry of equations (15)–(18), eigenvalue problem (28) is decomposed into eight eigenvalue problems for $N_t/8$ components of $\boldsymbol{x}$ with the values of (ℓ, m, n) in equation (29) corresponding to one of eight symmetry modes in expansions (19) and (20), called $\tilde{\boldsymbol{x}}$. Therefore, we examine the stability of the motionless state for the disturbance of each symmetry mode, similarly to the studies by Edwards (1988) and by Mizushima and Nakamura (2003). The eigenvalue problem for each symmetry mode can be written as

$$\tilde{A}\tilde{\boldsymbol{x}} = \sqrt{R_c}\tilde{B}\tilde{\boldsymbol{x}}, \tag{32}$$

where $\tilde{A}$ and $\tilde{B}$ are matrices of dimension $N_t/8$ obtained by keeping only non-zero components of matrices A and B, respectively. Equation (32) is rewritten as

$$C\tilde{\boldsymbol{x}} = \frac{1}{\sqrt{R_c}}\tilde{\boldsymbol{x}}, \tag{33}$$

where $C = \tilde{A}^{-1}\tilde{B}$.

The value of R_c for $\hat{\theta}(s_x, s_y, s_z)$ mode, obtained as the maximum eigenvalue of equation (33), is called $R_c^{(s_x,s_y,s_z)}$ hereinafter. Critical Rayleigh number R_c is defined as the minimum of $R_c^{(s_x,s_y,s_z)}$'s for all s_x, s_y and s_z. The symmetry mode corresponding to critical Rayleigh number is called the most unstable mode hereinafter. The velocity and temperature fields of most unstable mode are obtained from the eigenvector $\tilde{\boldsymbol{x}}$ of equation (33) for this mode associated with the eigenvalue corresponding to critical Rayleigh number.

4. Convergence of Numerical Solutions

The value of $R_c^{(s_x,s_y,s_z)}$ for truncation parameters (L, M, N) is expressed as $R_c^{[L,M,N]}$. Relative variations of $R_c^{[L,M,N]}$ with the increase in L, M and N by 1 are defined by

$$\begin{cases} \varepsilon_x^{[L,M,N]} = \dfrac{|R_c^{[L+1,M,N]} - R_c^{[L,M,N]}|}{R_c^{[L,M,N]}}, \\[2ex] \varepsilon_y^{[L,M,N]} = \dfrac{|R_c^{[L,M+1,N]} - R_c^{[L,M,N]}|}{R_c^{[L,M,N]}}, \\[2ex] \varepsilon_z^{[L,M,N]} = \dfrac{|R_c^{[L,M,N+1]} - R_c^{[L,M,N]}|}{R_c^{[L,M,N]}}, \end{cases} \tag{34}$$

respectively. Using these variables, maximum relative variation of $R_c^{[L,M,N]}$ at (L, M, N), $\varepsilon_{\max}^{[L,M,N]}$, is expressed as

$$\varepsilon_{\max}^{[L,M,N]} = \max\left(\varepsilon_x^{[L,M,N]}, \varepsilon_y^{[L,M,N]}, \varepsilon_z^{[L,M,N]}\right). \tag{35}$$

In the computation of $R_c^{(s_x,s_y,s_z)}$, we start with $L = M = N = 3$ or 4. We then repeat the procedure that L (or M, N) is increased by 1 if $\varepsilon_{\max}^{[L,M,N]} = \varepsilon_x^{[L,M,N]}$ (or $\varepsilon_{\max}^{[L,M,N]} = \varepsilon_y^{[L,M,N]}$, $\varepsilon_z^{[L,M,N]}$). We observe that $\varepsilon_{\max}^{[L,M,N]}$ tends to decrease to 0 and $R_c^{[L,M,N]}$ approaches a certain value, with the increase in $\sqrt{L^2+M^2+N^2}$ under this procedure. Examples of the dependence of $\varepsilon_{\max}^{[L,M,N]}$ on $\sqrt{L^2+M^2+N^2}$ for the most unstable mode are shown in figure 1 for $(A_x, A_y) = (0.025, 1), (0.1, 6)$ and $(0.025, 0.025)$. In this figure, roughly exponential decrease in $\varepsilon_{\max}^{[L,M,N]}$ with the increase in $\sqrt{L^2+M^2+N^2}$ is shown.

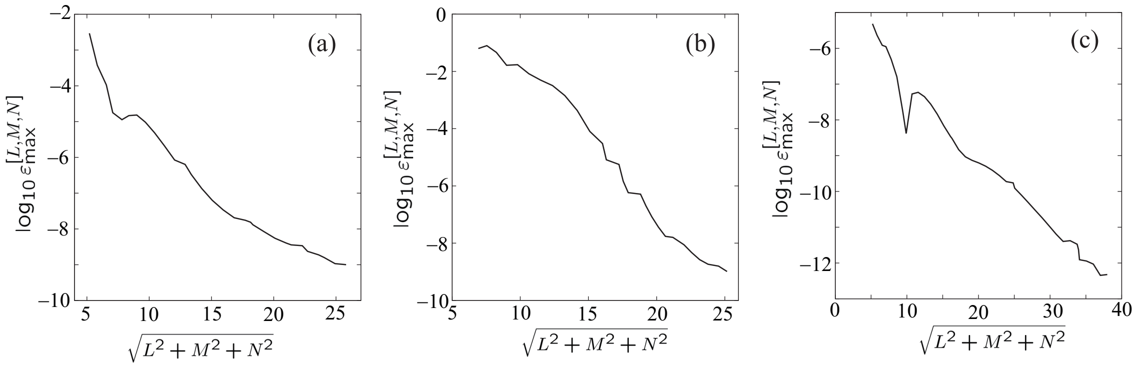

Figure 1. Examples of the dependence of $\varepsilon_{\max}^{[L,M,N]}$ on $\sqrt{L^2+M^2+N^2}$. (a): $(A_x, A_y) = (0.025, 1)$. $\hat{\theta}(e, o, e)$ mode. (b): $(A_x, A_y) = (0.1, 6)$. $\hat{\theta}(e, e, e)$ mode. (c): $(A_x, A_y) = (0.025, 0.025)$. $\hat{\theta}(e, o, e)$ mode.

In most calculations of $R_c^{(s_x,s_y,s_z)}$, the values of (L, M, N) are increased under the above procedure until $N_t/8$ reaches about 7000. For A_x and A_y satisfying $0.1 \le A_x, A_y \le 6$ or $0.01 \le A_x \le 0.1$ and $0.01 \le A_y \le 1$, $\varepsilon_{\max}^{[L,M,N]}$ reduces to 10^{-9} or less for the final value of (L, M, N) called (L_m, M_m, N_m). Therefore, the values of $R_c^{[L_m,M_m,N_m]}$ for these A_x and A_y are regarded as $R_c^{(s_x,s_y,s_z)}$. Here it is noted that the values of (L_m, M_m, N_m) strongly depend on aspect ratios A_x and A_y and the symmetry of the mode considered, probably reflecting the difference in the geometrical structures of velocity and temperature fields in the x, y and z directions. This dependence will be discussed in the next section.

Velocity field of $\hat{\theta}(s_x, s_y, s_z)$ mode denoted by $\hat{\boldsymbol{u}}^{(s_x,s_y,s_z)}$ is determined from equation (19) by using expansion coefficients $a_{(\ell,m,n)}^{(J)}$ obtained from eigenvector $\tilde{\boldsymbol{x}}$ of equation (33) for $\hat{\theta}(s_x, s_y, s_z)$ mode associated with the maximum eigenvalue. In order to examine the convergence of velocity fields with the increase in truncation parameters, a measure of difference in velocity fields for different truncation parameters, $\varepsilon_{\boldsymbol{u}}^{[L,M,N]}$, defined by

$$\varepsilon_{\boldsymbol{u}}^{[L,M,N]} = \frac{\max\limits_{x,y,z}\left|\hat{\boldsymbol{u}}^{[\tilde{L},\tilde{M},\tilde{N}]}(x,y,z) - \hat{\boldsymbol{u}}^{[L,M,N]}(x,y,z)\right|}{\max\limits_{x,y,z}\left|\hat{\boldsymbol{u}}^{[L,M,N]}(x,y,z)\right|}, \tag{36}$$

is introduced. Here $\hat{\boldsymbol{u}}^{[L,M,N]}$ and $\hat{\boldsymbol{u}}^{[\tilde{L},\tilde{M},\tilde{N}]}$ are the velocity fields for truncation parameters (L, M, N) and $(\tilde{L}, \tilde{M}, \tilde{N})$, respectively. Also $(\tilde{L}, \tilde{M}, \tilde{N})$ are the values of truncation parameters after three repetitions of the aforementioned procedure from (L, M, N),

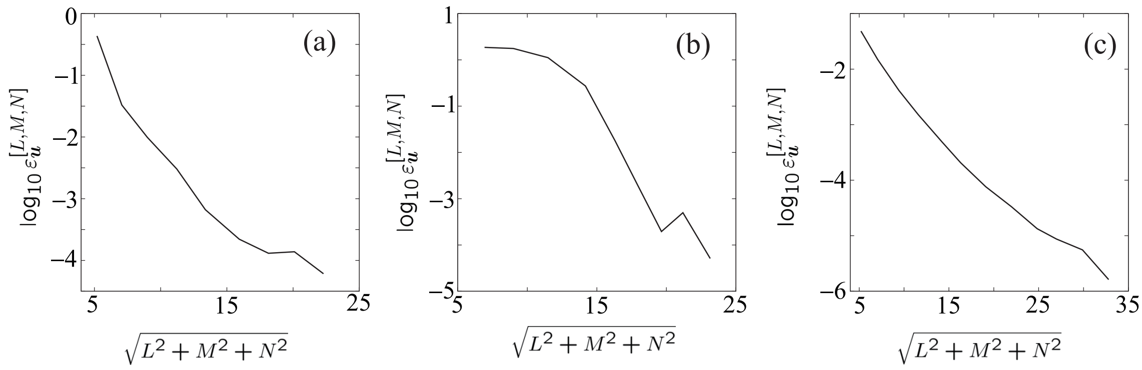

Figure 2. Examples of the dependence of $\varepsilon_{\boldsymbol{u}}^{[L,M,N]}$ on $\sqrt{L^2+M^2+N^2}$. (a): $(A_x, A_y) = (0.025, 1)$. $\hat{\theta}(e, o, e)$ mode. (b): $(A_x, A_y) = (0.1, 6)$. $\hat{\theta}(e, e, e)$ mode. (c): $(A_x, A_y) = (0.025, 0.025)$. $\hat{\theta}(e, o, e)$ mode.

which implies $\tilde{L} + \tilde{M} + \tilde{N} = L + M + N + 3$. $\varepsilon_{\boldsymbol{u}}^{[L,M,N]}$ tends to decrease exponentially as $\sqrt{L^2+M^2+N^2}$ increases, as illustrated in figure 2 for the most unstable modes for $(A_x, A_y) = (0.025, 1), (0.1, 6)$ and $(0.025, 0.025)$. Since the values of $\varepsilon_{\boldsymbol{u}}^{[L_m,M_m,N_m]}$ are 10^{-4} or less for any A_x and A_y satisfying $0.1 \leq A_x, A_y \leq 6$ or $0.025 \leq A_x \leq 0.1$ and $0.025 \leq A_y \leq 1$, the velocity field $\hat{\boldsymbol{u}}^{[L_m,M_m,N_m]}$ for these A_x and A_y is regarded as $\hat{\boldsymbol{u}}^{(s_x,s_y,s_z)}$.

5. Numerical Results

In this section, we show the results of numerical examination of R_c and the velocity field of most unstable mode both for $A_x \leq 1$ and $1 \leq A_y \leq 6$ and for $A_x = A_y \leq 1$.

5.1. The case of $A_x \leq 1$ and $1 \leq A_y \leq 6$

If A_x is decreased from 1 with A_y being fixed to a value between 1 and 6, we observe frequent changes of the symmetry of most unstable mode between $\hat{\theta}(e, e, e)$ and $\hat{\theta}(e, o, e)$ modes, as shown in figure 3. The changes occur more frequently for smaller A_x or for larger A_y.

As found from Table 1, R_c increases rapidly as A_x decreases to 0, whereas its dependence on A_y is relatively weak. Figure 4(a) shows the dependence of $R_c A_x^4$ for $\hat{\theta}(e, o, e)$ and $\hat{\theta}(e, e, e)$ modes on A_x for $A_y = 1$. The changes of the symmetry of most unstable mode occur three times for A_x between 0.025 and 0.1, although the change at the smallest A_x is not shown clearly in figure 4(a). The curve of $R_c A_x^4$ defined by $\min[R_c^{(e,o,e)} A_x^4, R_c^{(e,e,e)} A_x^4]$ in figure 4(a) tends to a finite non-zero value as A_x decreases to 0. Therefore, R_c is expected to be approximately proportional to A_x^{-4} for sufficiently small A_x. Figure 4(b) shows the dependence of $R_c A_x^4/\pi^4$ on A_x for fixed A_y of 1, 3 or 6. We observe that $R_c A_x^4$ tends to π^4 as A_x decreases to 0 irrespective of the value of A_y. Therefore, R_c is well approximated by $\pi^4 A_x^{-4}$ for small A_x for any A_y of O(1). This asymptotic behavior of R_c will be explained analytically in section 6.

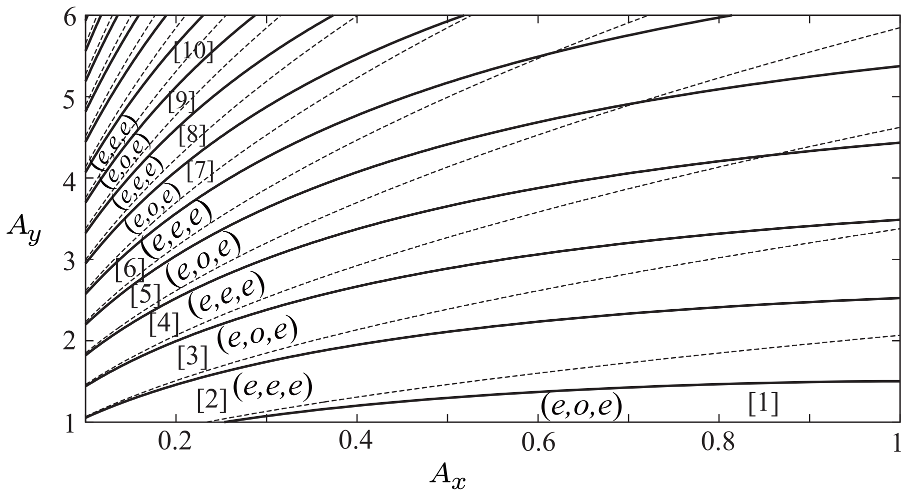

Figure 3. Symmetry of $\hat{\theta}$ of most unstable mode for $0.1 \le A_x \le 1$ and $1 \le A_y \le 6$. Solid lines denote the boundaries of the regions of symmetry $\hat{\theta}(e,e,e)$ and $\hat{\theta}(e,o,e)$ in the numerical computations. Broken lines are the boundaries of these regions obtained in the asymptotic analysis. Numbers in [ ] denote the number N_v of convection rolls of most unstable mode in the numerical computations.

Table 1. R_c and the symmetry of most unstable mode for a few typical aspect ratios with small A_x.

A_x	A_y	R_c	symmetry	(L_m, M_m, N_m)
0.5	6	9.126607×10^3	$\hat{\theta}(e,e,e)$	$(9,12,13)$
0.5	3	9.652946×10^3	$\hat{\theta}(e,e,e)$	$(9,11,14)$
0.5	1	1.497133×10^4	$\hat{\theta}(e,o,e)$	$(9,12,13)$
0.1	6	1.320239×10^6	$\hat{\theta}(e,e,e)$	$(4,19,16)$
0.1	3	1.327313×10^6	$\hat{\theta}(e,e,e)$	$(5,14,19)$
0.1	1	1.398958×10^6	$\hat{\theta}(e,e,e)$	$(5,14,19)$
0.025	1	2.690256×10^8	$\hat{\theta}(e,o,e)$	$(4,11,23)$

The flow pattern of most unstable mode for $A_x \ll 1$ and $A_y = \mathrm{O}(1)$ is a linear arrangement of several narrow convection rolls in the y direction, as illustrated in figure 5. In this figure, examples of the flow patterns of most unstable $\hat{\theta}(e,e,e)$ and $\hat{\theta}(e,o,e)$ modes for $A_x \ll 1$ and $A_y = 1$ composed of 4 and 5 narrow convection rolls are shown, respectively.

As found from figure 4(a), each change of the symmetry of most unstable mode with the decrease in A_x is associated with the increase in the number of convection rolls by one, which causes the decrease in their width-to-height ratio. The dependence of

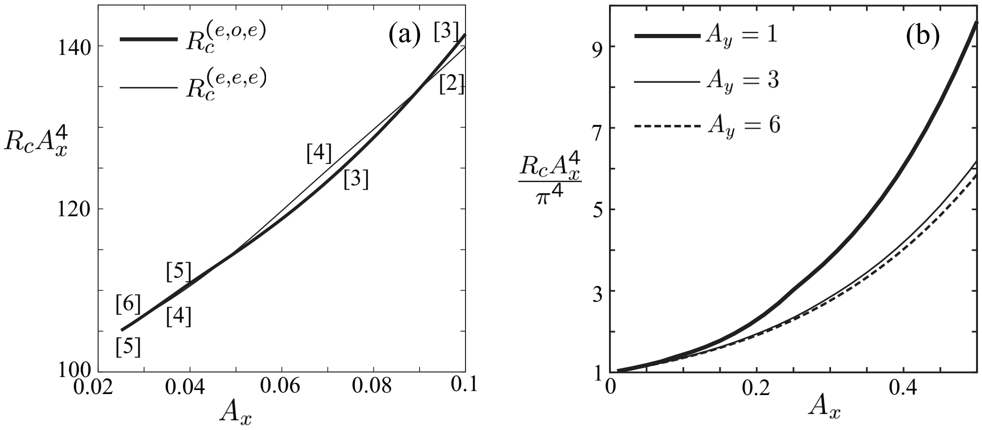

Figure 4. (a): Dependence of $R_c A_x^4$ for $\hat{\theta}(e,o,e)$ and $\hat{\theta}(e,e,e)$ modes on A_x. $A_y = 1$. Numbers in [ ] denote the number N_v of convection rolls of these modes. (b): Dependence of $R_c A_x^4/\pi^4$ on A_x for $A_y = 1, 3$ and 6.

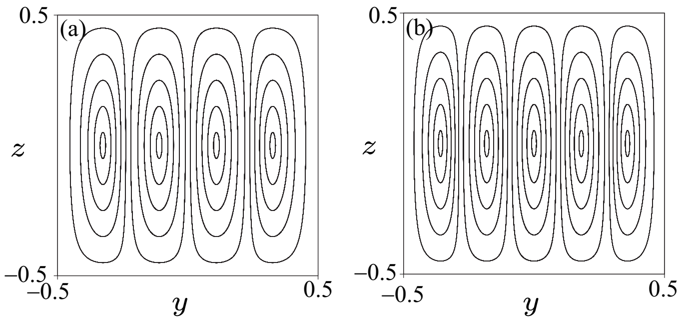

Figure 5. Trajectories of fluid particles on the symmetry plane $x = 0$. $A_y = 1$. (a): $A_x = 0.038$, $\hat{\theta}(e,e,e)$ mode. (b): $A_x = 0.025$, $\hat{\theta}(e,o,e)$ mode.

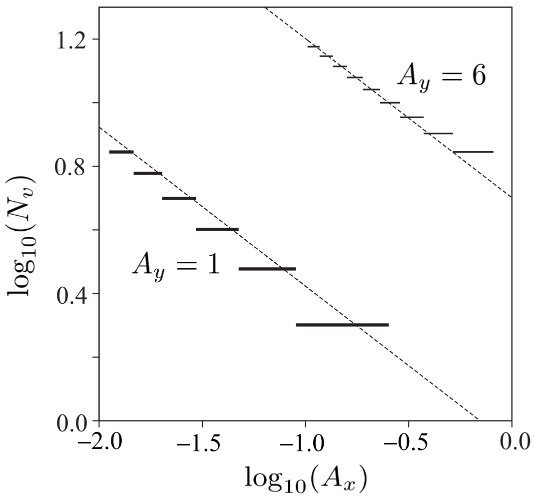

Figure 6. Dependence of the number N_v of convection rolls of most unstable mode on A_x. Thick and thin horizontal line segments denote the range of A_x within which the mode of N_v convection rolls is the most unstable for $A_y = 1$ and 6, respectively. Broken lines with slope $-1/2$ denote the value of N_v predicted in the asymptotic analysis.

the number N_v of convection rolls of the most unstable mode on A_x is shown in figure 6 for $A_y = 1$ and 6. At the end points of horizontal line segments of this figure, the changes of most unstable mode occur. Because these points are approximately along broken lines of slope $-1/2$, especially for very small A_x, we can say that N_v is roughly proportional to $1/\sqrt{A_x}$ if A_x is sufficiently small. That is, the horizontal length (or the width-to-height ratio) of each convection roll of the most unstable mode decreases with the decrease in A_x proportionally to $\sqrt{A_x}$.

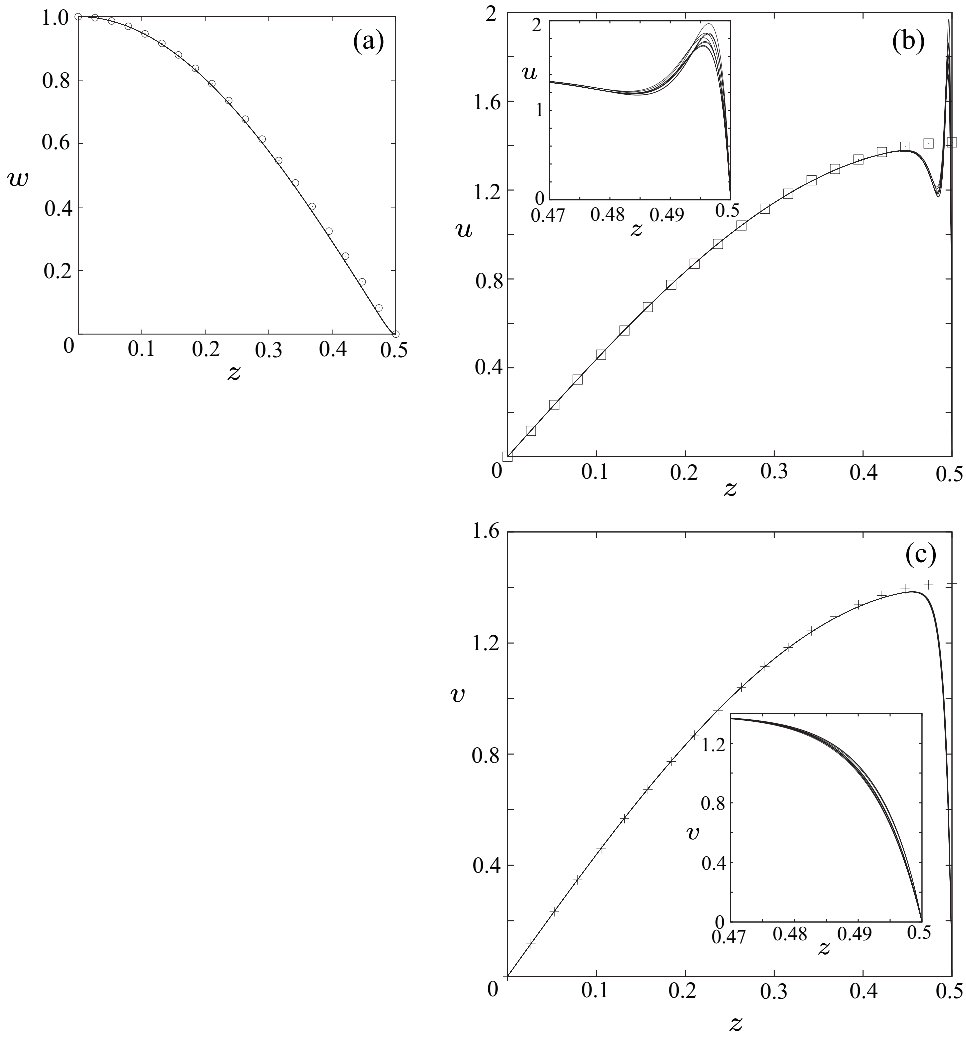

Figure 7. Superposition of the profiles expressing the z-dependences of normalized velocity components of most unstable mode at 9 locations of (x, y) where $x = A_x/8, A_x/4$ or $3A_x/8$ and $y = A_y/8, A_y/4$ or $3A_y/8$. $A_x = 0.025$ and $A_y = 1$. (a): Profiles of normalized w. (b): Profiles of normalized u. (c): Profiles of normalized v. In (b) and (c), magnifications of the profiles in the wall layer are shown in the insets. $\square, +$ and $\circ$ denote the profiles of normalized u, v and w, respectively, obtained in the asymptotic analysis.

Typical velocity profiles of the x, y and z components of $\hat{\boldsymbol{u}}$, u, v and w, of most unstable mode observed for $A_x \ll 1$ and $A_y = \mathrm{O}(1)$ are shown in figures 7, 8 and 9.

Figure 7 shows the normalized profiles expressing the z-dependences of these velocity components at 9 locations of (x, y) for $A_x = 0.025$ and $A_y = 1$. In figure 7(a), 9 profiles of the w normalized so that w is 1 at $z = 0$ are shown. Since these profiles are not distinguishable, the profile of normalized w is almost independent of (x, y).

In figure 7(b), u is normalized so that its value at $z = 0.25$ is 1. The profiles of normalized u at 9 locations of (x, y) are almost the same except in thin regions near the top and bottom walls. We call these regions (about $0.45 < z \leq 0.5$ in figure 7(b)) wall layers hereinafter. As z increases from 0, all the normalized u increase monotonically from 0, and approach a local maximum close to 1.4 near the outer edge of the wall layer. In the wall layer, however, the dependence of the profiles of normalized u on (x, y) is observed. As z increases from the outer edge of the wall layer, about 0.45 in figure 7(b), each of the normalized u first decreases to about 1.2, then increases to a maximum between 1.7 and 2.0, and finally rapidly decreases to 0.

Figure 7(c) shows the profiles of v normalized in the same way as u at 9 locations of (x, y). Similarly to the profiles of normalized u, the profiles of normalized v are almost independent of (x, y) except in the wall layers. As z increases from 0, all the normalized v monotonically increase to a value around 1.4 near the outer edge of the wall layer. However, within the wall layer, the normalized v is weakly dependent on (x, y) and rapidly decreases to 0 as z approaches 0.5.

For $A_x \ll 1$ and $A_y = \mathrm{O}(1)$, because of the rapid variations of u and v in the wall layers shown in figures 7(b) and (c), large truncation parameter N in the z direction is required for the computation with high accuracy. It is also found that the width of the wall layers, which is about 0.05 for $A_x = 0.025$, decreases with the decrease in A_x. Therefore, larger N_m is necessary in the numerical computations for smaller A_x, as illustrated in Table 1.

The x-dependences of normalized u, v and w of most unstable mode at 9 locations of (y, z) outside the wall layers for $A_x = 0.025$ and $A_y = 1$ are shown in figure 8. Here u is normalized so that it is 1 at $x = A_x/4$, whereas v and w are normalized so that they are 1 at $x = 0$. Because the 9 lines of profiles of each velocity component are not distinguishable, the profiles of normalized u, v and w are almost independent of y and z outside the wall layers. Normalized v and w take a maximum at $x = 0$ and monotonically decrease to 0 as side walls $x = \pm A_x/2$ are approached, whereas normalized u takes a maximum near $x = \pm A_x/4$.

Figure 9 shows the y-dependences of normalized u, v and w of most unstable mode at 9 locations of (x, z) outside the wall layers for $A_y = 1$. Here the profiles of each component of velocity are normalized so that their maxima in the region of $0 \leq y \leq 0.5$ is 1. The 9 lines of profiles of each velocity component are again not distinguishable, which suggests that the profiles of normalized u, v and w are almost independent of x and z outside the wall layers. For $A_x = 0.038$, $\hat{\theta}(e, e, e)$ mode is most unstable, in which u and w are even functions of y as shown in figures 9(c) and (a), whereas v is an odd function of y as shown in figure 9(e). However, for $A_x = 0.025$, $\hat{\theta}(e, o, e)$ mode is most unstable, which causes the opposite parity of velocity components with respect to $y = 0$,

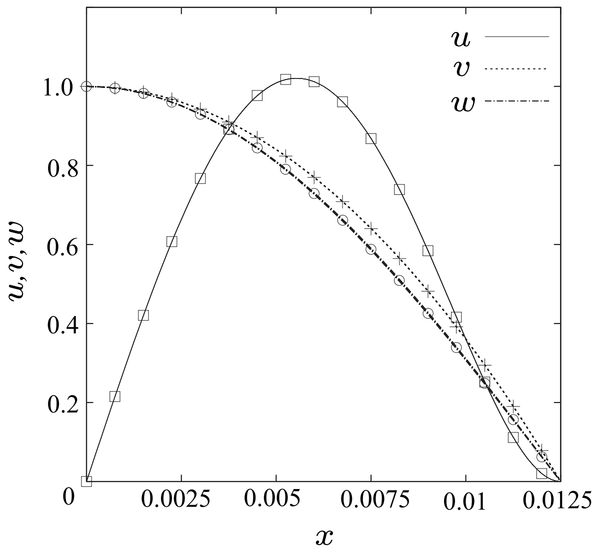

Figure 8. Superposition of the profiles expressing the x-dependences of normalized u, v and w of most unstable mode at 9 locations of (y, z) where $y = A_y/8, A_y/4$ or $3A_y/8$ and $z = 1/8, 1/4$ or $3/8$. $A_x = 0.025$ and $A_y = 1$. $\square, +$ and $\circ$ denote the profiles of normalized u, v and w, respectively, obtained in the asymptotic analysis.

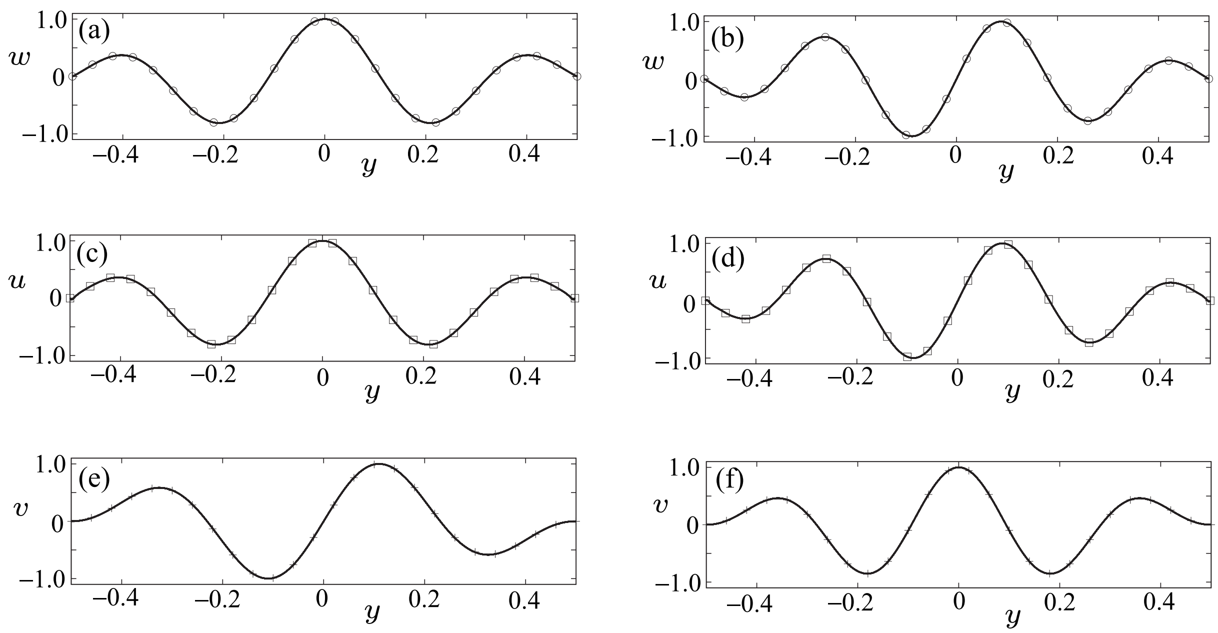

Figure 9. Superposition of the profiles expressing the y-dependences of normalized velocity components of most unstable mode at 9 locations of (x, z) where $x = A_x/8, A_x/4$ or $3A_x/8$ and $z = 1/8, 1/4$ or $3/8$. $A_y = 1$. (a), (c) and (e): $A_x = 0.038$, (b), (d) and (f): $A_x = 0.025$. (a) and (b): Profiles of normalized w. (c) and (d): Profiles of normalized u. (e) and (f): Profiles of normalized v. $\square, +$ and $\circ$ denote the profiles of normalized u, v and w, respectively, obtained in the asymptotic analysis.

as found from figures 9(b), (d) and (f). The vertical flows in the flow patterns shown in figure 5 are weaker near the shorter side walls $y = \pm A_y/2$ than those near the central plane $y = 0$, as found from figures 9(a) and (b). The same tendency is observed also for u and v. It is also noted that the profiles of normalized u and w are almost the same, as found from figures 9(a)–(d).

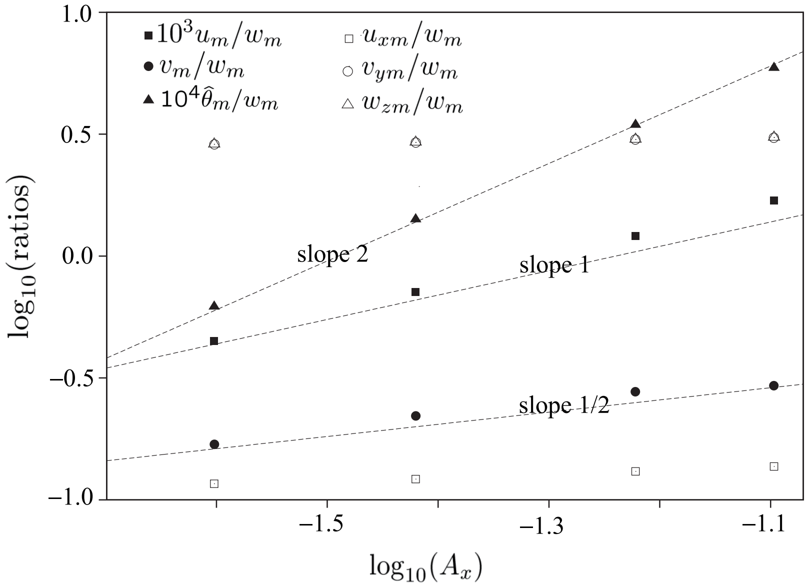

Figure 10. Dependences of the ratios of u_m, v_m, $\hat{\theta}_m$, u_{xm}, v_{ym} and w_{zm} to w_m on A_x. $A_y = 1$. Broken lines are the lines of slopes 2, 1 and 1/2.

The ratios of representative magnitudes of u, v, w and $\hat{\theta}$ or their spatial derivatives of the most unstable mode for $A_x \ll 1$ and $A_y = \mathrm{O}(1)$ are also examined. Figure 10 shows the dependences of the ratios of u_m, v_m, $\hat{\theta}_m$, u_{xm}, v_{ym} and w_{zm} to w_m on A_x for $A_y = 1$, where $u_m, v_m, w_m, \hat{\theta}_m, u_{xm}, v_{ym}$ and w_{zm} are the values of $|u|, |v|, |w|, |\hat{\theta}|, |\partial u/\partial x|, |\partial v/\partial y|$ and $|\partial w/\partial z|$ averaged over the x, y and z in the cavity, respectively. Because u_m is much smaller than v_m and w_m, the assumption of finite roll adopted by Davis (1967) is a good approximation for $A_x \ll 1$ and $A_y = \mathrm{O}(1)$. We also find that u_m/w_m, v_m/w_m and $\hat{\theta}_m/w_m$ decrease with the decrease in A_x proportionally to A_x, $\sqrt{A_x}$ and A_x^2, respectively. However, u_{xm}/w_m, v_{ym}/w_m and w_{zm}/w_m are almost independent of A_x. These dependences of several ratios on A_x will be used in the asymptotic analysis of section 6.

5.2. *The case of $A_x = A_y = A < 1$*

In this subsection, we consider the onset of thermal convection in the cavity of a square base with $A_x = A_y = A < 1$. For these aspect ratios, both $\hat{\theta}(e, o, e)$ and $\hat{\theta}(o, e, e)$ modes are most unstable. Critical Rayleigh number R_c increases rapidly as A decreases to 0, as illustrated in Table 2. Moreover, R_c is well approximated by $25\pi^4 A^{-4}$ for sufficiently

Table 2. R_c and the symmetry of most unstable mode for a few aspect ratios satisfying $A_x = A_y = A < 1$.

A	R_c	symmetry	(L_m, M_m, N_m)
0.5	4.941374×10^4	$\hat{\theta}(e, o, e)$	$(11, 9, 15)$
0.1	2.454351×10^7	$\hat{\theta}(e, o, e)$	$(8, 7, 25)$
0.025	6.237110×10^9	$\hat{\theta}(e, o, e)$	$(5, 7, 37)$

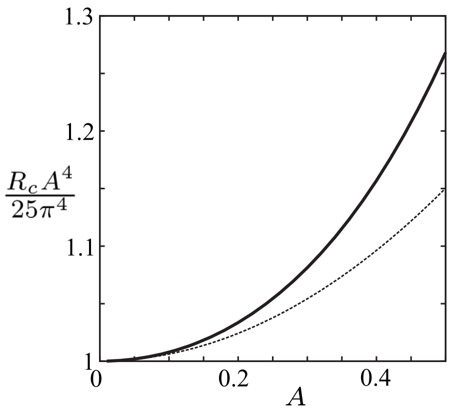

Figure 11. Dependence of $R_cA^4/(25\pi^4)$ on A. Solid line denotes the numerical result. Broken line is the result of the asymptotic analysis.

small A, as found from the solid line in figure 11. This asymptotic behavior of R_c will be explained analytically in section 6.

The flow pattern of most unstable $\hat{\theta}(e, o, e)$ [$\hat{\theta}(o, e, e)$] mode for small A is composed of only one convection roll whose width-to-height ratio is small, and whose axis is parallel to the x axis [y axis]. An example of this flow pattern for $\hat{\theta}(e, o, e)$ mode is shown in figure 12 for $A = 0.0625$. In this figure, the trajectories starting from non-zero x are not on the planes of constant x but are slightly curved if they are projected onto the xy plane. The result suggesting the flow pattern of most unstable mode composed of a narrow convection roll for small A was obtained also by Davis (1967) under the assumption of finite roll.

Typical profiles of the velocity components of most unstable $\hat{\theta}(e, o, e)$ mode for $A \ll 1$ are shown in figure 13. Figure 13(a) shows the z-dependences of normalized u, v and w at 9 locations of (x, y). Here u and v are normalized so that their values at $z = 0.25$ is 1, whereas w is normalized so that it is 1 at $z = 0$. Since the 9 dotted-broken lines in this figure are not distinguishable, the profile of normalized w is almost independent of (x, y).

The 9 profiles of normalized u are almost the same except in thin regions near the

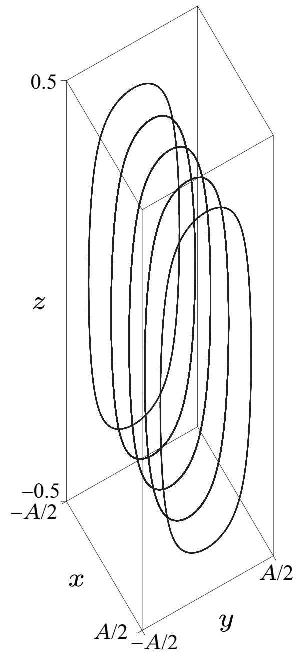

Figure 12. Trajectories of fluid particles starting from 5 points on the line of $y = 0$ and $z = 0.4$ in the velocity field of most unstable $\hat{\theta}(e, o, e)$ mode. $A = 0.0625$.

top and bottom walls, as found from figure 13(a). We again call these regions (about $0.43 < z \leq 0.5$ in figure 13(a)) wall layers. With the increase in z from 0, all the normalized u increases monotonically and approaches a local maximum around 1.4 as z approaches the outer edge of the wall layer. Within the wall layers, however, the dependence of the profiles of normalized u on (x, y) is observed. With the increase in z from the outer edge of the wall layer to 0.5, each of these profiles first decreases to a local minimum, then takes a maximum at z around 0.49, and finally decreases rapidly to 0.

Outside the wall layer, the broken curves of normalized v are hidden behind the solid curves of normalized u in figure 13(a). Therefore, the profiles of normalized v outside the wall layer are very close to the profiles of normalized u, and are almost independent of (x, y). However, the normalized v in the wall layer is weakly dependent on (x, y), as found from the inset of this figure.

Because of the rapid variations of u and v in the wall layers shown in figure 13(a), large truncation parameter N in the z direction is again required for the computation of high accuracy for $A \ll 1$. It is also found that the width of the wall layers, which is about 0.07 for $A = 0.0625$, decreases as A decreases. Therefore, for smaller A, larger N_m is necessary for the numerical computations with sufficient accuracy, as illustrated in Table 2.

The x-dependences of u, v and w at 9 locations of (y, z) outside the wall layers are shown in figure 13(b). Here u is normalized so that it is 1 at $x = A/4$, whereas v and w are normalized so that they are 1 at $x = 0$. The profiles of the normalized w are almost

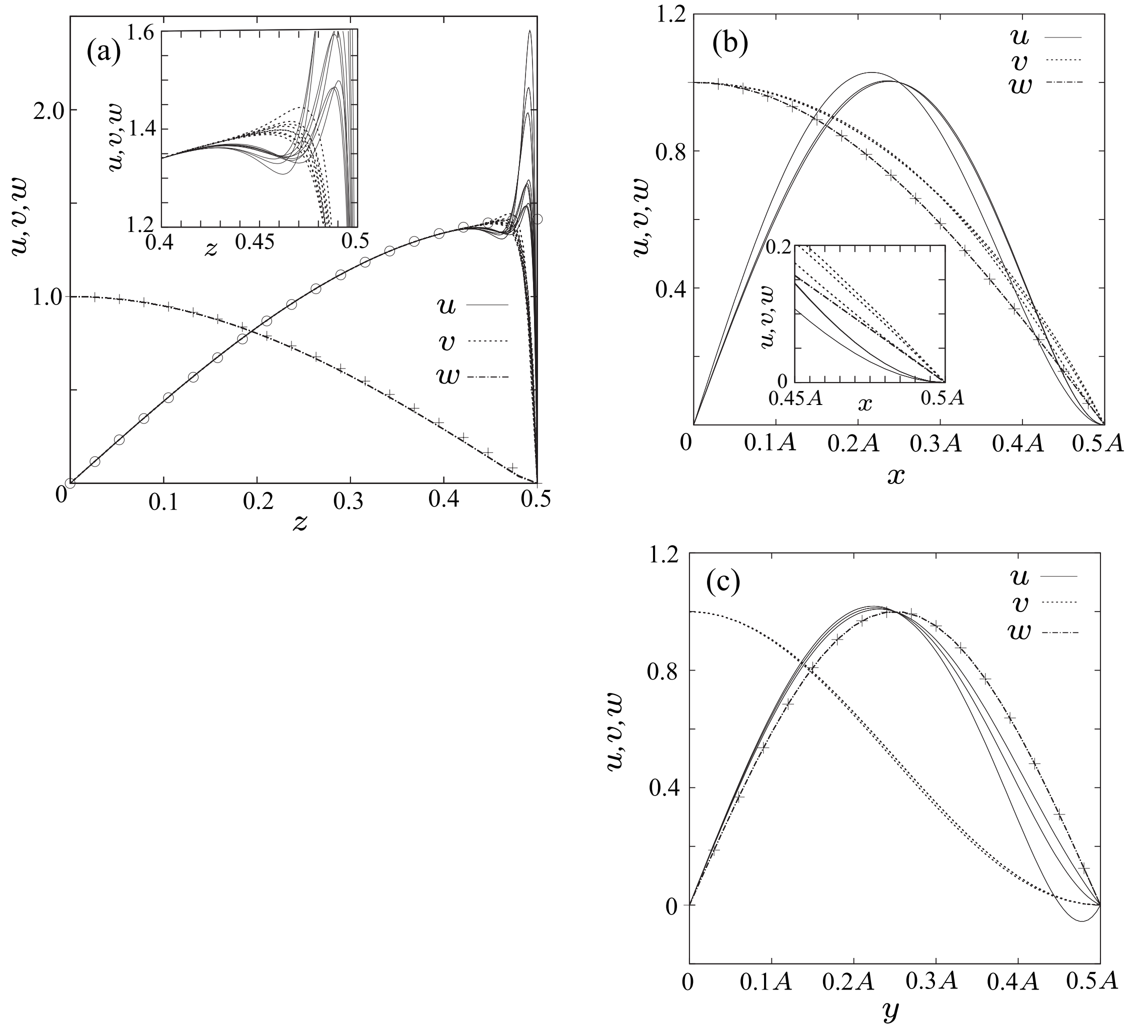

Figure 13. Superposition of profiles expressing the normalized velocity components of most unstable mode at several locations. $A = 0.0625$. (a): z-dependences of normalized u, v and w at 9 locations of (x, y) where $x = A/8, A/4$ or $3A/8$ and $y = A/8, A/4$ or $3A/8$. A magnification of the profiles in the wall layer is shown in the inset. (b): x-dependences of normalized u, v and w at 9 locations of (y, z) where $y = A/8, A/4$ or $3A/8$ and $z = 1/8, 1/4$ or $3/8$. A magnification of the profiles is shown in the inset. (c): y-dependences of normalized u, v and w at 9 locations of (x, z) where $x = A/8, A/4$ or $3A/8$ and $z = 1/8, 1/4$ or $3/8$. Symbols $+$ and $\circ$ denote the profiles of normalized w and normalized u and v obtained in the asymptotic analysis, respectively.

independent of y and z. However, three curves of profiles are observed for both the normalized u and v (three curves of normalized v are shown more clearly in the inset of figure 13(b)). These curves correspond to the profiles at the locations of three different y's because the profiles at the locations of same y are not distinguishable even if z is different. This observation suggests that the profiles of normalized u and v vary with y but are independent of z.

Figure 13(c) shows the y-dependences of u, v and w at 9 locations of (x, z) outside the wall layers. Here u and w are normalized so that they are 1 at $y = A/4$, whereas v is normalized so that it is 1 at $y = 0$. We first find that the profiles of normalized w are almost independent of (x, z). However, three curves of normalized u for different x are observed in figure 13(c) because the profiles for the same x are not distinguishable even if z is different. Therefore, it is suggested that the normalized u depends on x but is independent of z. The existence of a reverse flow region near $y = A/2$ in one of three curves of normalized u implies a little complicated flow field near the side walls of $y = \pm A/2$. The profiles of normalized v also depend only on x, although it is not easy to recognize this weak dependence in figure 13(c).

The ratios of $u_m, v_m, w_m, \hat{\theta}_m, u_{xm}, v_{ym}$ and w_{zm}, introduced in section 5.1, of the most unstable mode are examined also for $A \ll 1$. Figure 14 shows the dependences of the ratios of u_m, v_m, $\hat{\theta}_m$, u_{xm}, v_{ym} and w_{zm} to w_m on A. Because u_m is much smaller than v_m and w_m, the assumption of finite roll is a good approximation also for $A \ll 1$. We also find that both u_m/w_m and v_m/w_m decrease with the decrease in A proportionally to A. However, $\hat{\theta}_m/w_m$ decreases with the decrease in A proportionally to A^2. The ratios u_{xm}/w_m, v_{ym}/w_m and w_{zm}/w_m are almost independent of A. From the above results, we can say that although the dependence of v_m/w_m on A for $A \ll 1$ is different from its dependence on A_x for $A_x \ll 1$ and $A_y = \mathrm{O}(1)$, the dependences of other ratios on A for $A \ll 1$ are the same as those on A_x for $A_x \ll 1$ and $A_y = \mathrm{O}(1)$.

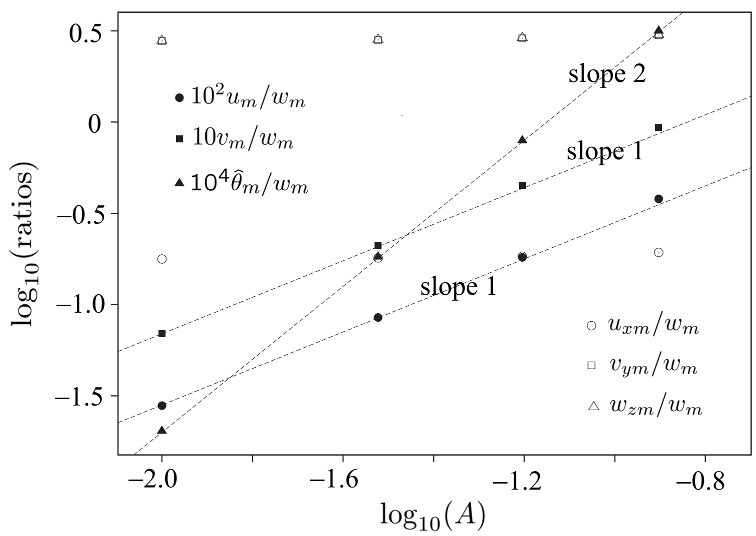

Figure 14. Dependences of the ratios of u_m, v_m, $\hat{\theta}_m$, u_{xm}, v_{ym} and w_{zm} to w_m on A. Broken lines are lines of slopes 1 and 2.

6. Asymptotic analysis

From equations (15)–(17), we can obtain the following equations:

$$\frac{\partial u}{\partial x} + \frac{\partial v}{\partial y} + \frac{\partial w}{\partial z} = 0, \tag{37}$$

$$\frac{\partial}{\partial y}\Delta u - \frac{\partial}{\partial x}\Delta v = 0, \tag{38}$$

$$\frac{\partial}{\partial z}\Delta u - \frac{\partial}{\partial x}\Delta w - R_c\frac{\partial \hat{\theta}}{\partial x} = 0, \tag{39}$$

$$\frac{\partial}{\partial z}\Delta v - \frac{\partial}{\partial y}\Delta w - R_c\frac{\partial \hat{\theta}}{\partial y} = 0, \tag{40}$$

$$\Delta\hat{\theta} + w = 0, \tag{41}$$

where u, v and w are the x, y and z components of $\hat{\boldsymbol{u}}$, respectively. Boundary condition (18) is rewritten as

$$u = v = w = \hat{\theta} = 0 \quad \text{on } x = \pm\frac{A_x}{2}, \text{ on } y = \pm\frac{A_y}{2}, \text{ and on } z = \pm\frac{1}{2}. \tag{42}$$

6.1. The case of $A_x \ll 1$

Most of the numerical results for $A_x \ll 1$ and $A_y = \mathrm{O}(1)$ shown in section 5.1 can be explained by using an asymptotic analysis if we adopt a few assumptions based on the numerical results, as will be shown below. In consideration of the numerical results shown in figures 4 and 10, we assume that $u, v, w, \hat{\theta}$ and R_c are expressed as

$$\begin{cases} u = A_x(\tilde{u}_0 + A_x\tilde{u}_1), \ v = \sqrt{A_x}(\tilde{v}_0 + A_x\tilde{v}_1), \ w = \tilde{w}_0 + A_x\tilde{w}_1, \\ \hat{\theta} = A_x^2(\tilde{\theta}_0 + A_x\tilde{\theta}_1), \ R_c = A_x^{-4}(\tilde{R}_0 + A_x\tilde{R}_1), \end{cases} \tag{43}$$

for small A_x, where functions $\tilde{u}_0, \tilde{v}_0, \tilde{w}_0, \tilde{\theta}_0, \tilde{u}_1, \tilde{v}_1, \tilde{w}_1$ and $\tilde{\theta}_1$ are independent of A_x, and $\tilde{R}_0$ and $\tilde{R}_1$ are constants independent of A_x. It is also assumed that these functions depend on

$$\tilde{x} \equiv \frac{1}{A_x}x, \quad \tilde{y} \equiv \frac{1}{\sqrt{A_x}}y, \tag{44}$$

and z, because the representative scale of $\hat{\boldsymbol{u}}$ and $\hat{\theta}$ in the x direction is expected to be of $\mathrm{O}(A_x)$, and because the numerical result shown in figure 10 suggests that their representative scale in the y direction is of $\mathrm{O}(\sqrt{A_x})$.

If we substitute equation (43) into equation (41), we obtain

$$\tilde{w}_0 = -\frac{\partial^2\tilde{\theta}_0}{\partial\tilde{x}^2}, \tag{45}$$

at the leading order of A_x, and

$$\tilde{w}_1 = -\frac{\partial^2\tilde{\theta}_1}{\partial\tilde{x}^2} - \frac{\partial^2\tilde{\theta}_0}{\partial\tilde{y}^2}, \tag{46}$$

at the next order of A_x. Moreover, substituting equation (43) into equations (38)–(40), we obtain

$$\frac{\partial^3\tilde{v}_0}{\partial\tilde{x}^3} = 0, \tag{47}$$

$$\frac{\partial^3\tilde{w}_0}{\partial\tilde{x}^3} + \tilde{R}_0\frac{\partial\tilde{\theta}_0}{\partial\tilde{x}} = 0, \tag{48}$$

$$\frac{\partial^3 \tilde{w}_0}{\partial \tilde{x}^2 \partial \tilde{y}} + \tilde{R}_0 \frac{\partial \tilde{\theta}_0}{\partial \tilde{y}} = 0, \tag{49}$$

at the leading order, and

$$\frac{\partial^3 \tilde{v}_1}{\partial \tilde{x}^3} + \frac{\partial^3 \tilde{v}_0}{\partial \tilde{x} \partial \tilde{y}^2} - \frac{\partial^3 \tilde{u}_0}{\partial \tilde{x}^2 \partial \tilde{y}} = 0, \tag{50}$$

$$\frac{\partial}{\partial \tilde{x}} \left(\frac{\partial^2 \tilde{w}_1}{\partial \tilde{x}^2} + \frac{\partial^2 \tilde{w}_0}{\partial \tilde{y}^2} \right) + \tilde{R}_1 \frac{\partial \tilde{\theta}_0}{\partial \tilde{x}} + \tilde{R}_0 \frac{\partial \tilde{\theta}_1}{\partial \tilde{x}} = 0, \tag{51}$$

$$-\frac{\partial^3 \tilde{v}_0}{\partial \tilde{x}^2 \partial z} + \frac{\partial}{\partial \tilde{y}} \left(\frac{\partial^2 \tilde{w}_1}{\partial \tilde{x}^2} + \frac{\partial^2 \tilde{w}_0}{\partial \tilde{y}^2} \right) + \tilde{R}_1 \frac{\partial \tilde{\theta}_0}{\partial \tilde{y}} + \tilde{R}_0 \frac{\partial \tilde{\theta}_1}{\partial \tilde{y}} = 0, \tag{52}$$

at the next order. Substitution of equation (43) into equation (37) yields

$$\frac{\partial \tilde{u}_0}{\partial \tilde{x}} + \frac{\partial \tilde{v}_0}{\partial \tilde{y}} + \frac{\partial \tilde{w}_0}{\partial z} = 0, \tag{53}$$

at the leading order. From boundary condition (42), we obtain

$$\tilde{u}_j = \tilde{v}_j = \tilde{w}_j = \tilde{\theta}_j = 0 \quad (j = 0, 1) \quad \text{on} \quad \tilde{x} = \pm\frac{1}{2}, \tag{54}$$

$$\tilde{u}_j = \tilde{v}_j = \tilde{w}_j = \tilde{\theta}_j = 0 \quad (j = 0, 1) \quad \text{on} \quad z = \pm\frac{1}{2}. \tag{55}$$

Using equations (45) and (48), the differential equation

$$\frac{\partial^4 \tilde{w}_0}{\partial \tilde{x}^4} - \tilde{R}_0 \tilde{w}_0 = 0, \tag{56}$$

for $\tilde{w}_0$ is derived. Here, the numerical results shown in figures 7–9 suggest that for small A_x, w can be expressed as a product of a function of $\tilde{x}$, a function of $\tilde{y}$ and a function of z except in the wall layers. Therefore, we assume that $\tilde{w}_0$ is expressed as

$$\tilde{w}_0 = \tilde{X}_w(\tilde{x}) \tilde{Y}_w(\tilde{y}) \tilde{Z}_w(z), \tag{57}$$

except in the wall layers, where $\tilde{X}_w, \tilde{Y}_w$ and $\tilde{Z}_w$ are functions of $\tilde{x}$, $\tilde{y}$ and z, respectively. From the equation obtained by substituting equation (57) into equation (56) and boundary condition (54), we find that $\tilde{X}_w$ should satisfy

$$\frac{d^4 \tilde{X}_w}{d\tilde{x}^4} = \tilde{R}_0 \tilde{X}_w,$$

$$\tilde{X}_w = 0 \quad \text{at} \quad \tilde{x} = \pm\frac{1}{2}.$$

The solution to these equations that gives the smallest $\tilde{R}_0$ is written as

$$\tilde{X}_w = \cos(\pi \tilde{x}), \tag{58}$$

for which

$$\tilde{w}_0 = \cos(\pi \tilde{x}) \tilde{Y}_w(\tilde{y}) \tilde{Z}_w(z), \tag{59}$$

$$\tilde{R}_0 = \pi^4, \tag{60}$$

are obtained. Moreover, from equations (48), (54) and (59), the following expression of $\tilde{\theta}_0$ is derived:

$$\tilde{\theta}_0 = \frac{1}{\pi^2}\cos(\pi\tilde{x})\tilde{Y}_w(\tilde{y})\tilde{Z}_w(z). \tag{61}$$

Equation (49) is satisfied by the $\tilde{w}_0, \tilde{\theta}_0$ and $\tilde{R}_0$ obtained above.

The locations of side walls expressed by $y = \pm A_y/2$ correspond to $\tilde{y} \to \pm\infty$ in the limit of $A_x \to 0$ for fixed A_y. However, if the boundary condition for $\tilde{y} \to \pm\infty$ is imposed, the dependence of velocity fields and R_c on A_y cannot be derived. Therefore, in the following analysis, we use the boundary condition

$$\tilde{u}_j = \tilde{v}_j = \tilde{w}_j = \tilde{\theta}_j = 0 \quad (j = 0, 1) \quad \text{on} \quad \tilde{y} = \pm\tilde{y}_b, \tag{62}$$

where $\tilde{y}_b = A_y/(2\sqrt{A_x})$ is assumed to be independent of A_x. This assumption means that we consider the limit of $A_x \to 0$ with $A_y = \mathrm{O}(\sqrt{A_x})$ instead of $A_y = \mathrm{O}(1)$.

Using equations (47) and (53) and boundary conditions (54) and (62), we obtain

$$\tilde{u}_0 = -\frac{1}{\pi}[4\tilde{x}^3 - 3\tilde{x} + \sin(\pi\tilde{x})]\tilde{Y}_w(\tilde{y})\frac{d\tilde{Z}_w(z)}{dz}, \tag{63}$$

$$\tilde{v}_0 = \frac{12}{\pi}\left(\tilde{x}^2 - \frac{1}{4}\right)\frac{d\tilde{Z}_w(z)}{dz}\int_{-\tilde{y}_b}^{\tilde{y}} \tilde{Y}_w(\tilde{y}')d\tilde{y}'. \tag{64}$$

The following equations are derived from boundary conditions (55) and (62) and equations (59), (63) and (64):

$$\tilde{Z}_w = 0 \quad \text{at} \quad z = \pm\frac{1}{2}, \tag{65}$$

$$\frac{d\tilde{Z}_w}{dz} = 0 \quad \text{at} \quad z = \pm\frac{1}{2}, \tag{66}$$

$$\tilde{Y}_w = 0 \quad \text{at} \quad \tilde{y} = \pm\tilde{y}_b, \tag{67}$$

$$\int_{-\tilde{y}_b}^{\tilde{y}_b} \tilde{Y}_w(\tilde{y}')d\tilde{y}' = 0. \tag{68}$$

However, because we consider only the velocity field outside the wall layers, taking account of the z-dependences of u, v and w in the numerical computation shown in figure 7, we use only equation (65) as the boundary condition for $\tilde{Z}_w$ at $z = \pm 1/2$.

At the next order of A_x, from equations (46), (51), (54) and (59)–(61), we obtain

$$\tilde{\theta}_1 = \cos(\pi\tilde{x})c_1(\tilde{y}, z) + \frac{1}{8\pi^5}\left[2 - \frac{\cosh(\pi\tilde{x})}{\cosh(\pi/2)} - 2\tilde{x}\sin(\pi\tilde{x})\right]\left(\tilde{R}_1\tilde{Y}_w + 2\pi^2\frac{d^2\tilde{Y}_w}{d\tilde{y}^2}\right)\tilde{Z}_w, \tag{69}$$

$$\tilde{w}_1 = \left[\pi^2 c_1(\tilde{y}, z) + \frac{\tilde{R}_1}{2\pi^4}\tilde{Y}_w\tilde{Z}_w\right]\cos(\pi\tilde{x}) + \frac{1}{8\pi^3}\left[\frac{\cosh(\pi\tilde{x})}{\cosh(\pi/2)} - 2\tilde{x}\sin(\pi\tilde{x})\right]\left(\tilde{R}_1\tilde{Y}_w + 2\pi^2\frac{d^2\tilde{Y}_w}{d\tilde{y}^2}\right)\tilde{Z}_w, \tag{70}$$

where c_1 is a function of $\tilde{y}$ and z. Using equations (52), (59)–(61), (64), (69) and (70), we obtain the following equation for $\tilde{Y}_w$ and $\tilde{Z}_w$:

$$\tilde{R}_1 \frac{d\tilde{Y}_w}{d\tilde{y}} \tilde{Z}_w + 2\pi^2 \frac{d^3\tilde{Y}_w}{d\tilde{y}^3} \tilde{Z}_w - 96 \frac{d^2\tilde{Z}_w}{dz^2} \int_{-\tilde{y}_b}^{\tilde{y}} \tilde{Y}_w(\tilde{y}') d\tilde{y}' = 0. \tag{71}$$

By the differentiation of equation (71) with respect to $\tilde{y}$, the equation

$$\tilde{R}_1 \frac{d^2\tilde{Y}_w}{d\tilde{y}^2} \tilde{Z}_w + 2\pi^2 \frac{d^4\tilde{Y}_w}{d\tilde{y}^4} \tilde{Z}_w - 96\tilde{Y}_w \frac{d^2\tilde{Z}_w}{dz^2} = 0, \tag{72}$$

is derived. From equation (72), we obtain the following two equations for $\tilde{Y}_w$ and $\tilde{Z}_w$:

$$2\pi^2 \frac{d^4\tilde{Y}_w}{d\tilde{y}^4} + \tilde{R}_1 \frac{d^2\tilde{Y}_w}{d\tilde{y}^2} - \kappa\tilde{Y}_w = 0, \tag{73}$$

$$96 \frac{d^2\tilde{Z}_w}{dz^2} - \kappa\tilde{Z}_w = 0, \tag{74}$$

where κ is a constant. Here, in consideration of equation (74) and boundary condition (65), it is reasonable to expect that $\tilde{Z}_w$ is expressed as

$$\tilde{Z}_w = \cos(\pi z), \tag{75}$$

because there is always only one convection cell in the vertical direction in the numerical flow pattern of most unstable mode, as illustrated in figure 5. Substituting equation (75) into equation (74), we obtain the relation $\kappa = -96\pi^2$, using which equation (73) is rewritten as

$$\frac{d^4\tilde{Y}_w}{d\tilde{y}^4} + \frac{\tilde{R}_1}{2\pi^2} \frac{d^2\tilde{Y}_w}{d\tilde{y}^2} + 48\tilde{Y}_w = 0. \tag{76}$$

In the case of $\tilde{y}_b \to \infty$, we can assume that $\tilde{Y}_w$ is expressed as

$$\tilde{Y}_w = \cos(k_0\tilde{y}), \tag{77}$$

where k_0 is a constant. Substitution of equation (77) into equation (76) yields

$$\tilde{R}_1 = 2k_0^2\pi^2 + \frac{96\pi^2}{k_0^2}.$$

Therefore, $\tilde{R}_1$ takes the minimum of

$$\tilde{R}_{1\infty} \equiv 16\sqrt{3}\pi^2, \tag{78}$$

when k_0 is equal to $2 \cdot 3^{\frac{1}{4}}$. However, for finite $\tilde{y}_b$, $\tilde{R}_1$ is expected to be larger than $\tilde{R}_{1\infty}$ because $\tilde{Y}_w$ is required to satisfy equations (67) and (68) as well as equation (76). From equations (68), (71) and (75), we obtain the boundary condition given by

$$\frac{d^3\tilde{Y}_w}{d\tilde{y}^3} + \frac{\tilde{R}_1}{2\pi^2} \frac{d\tilde{Y}_w}{d\tilde{y}} = 0 \quad \text{at} \quad \tilde{y} = \pm\tilde{y}_b. \tag{79}$$

Odd and even functions satisfying equation (76) are expressed as

$$\tilde{Y}_w = a_1 \sin(\mu_1\tilde{y}) + a_2 \sin(\mu_2\tilde{y}), \tag{80}$$

and

$$\tilde{Y}_w = b_1 \cos(\mu_1 \tilde{y}) + b_2 \cos(\mu_2 \tilde{y}), \tag{81}$$

respectively, where

$$\mu_j = \frac{1}{2\pi}\sqrt{\tilde{R}_1 - (-1)^j \sqrt{\tilde{R}_1^2 - \tilde{R}_{1\infty}^2}} \quad (j = 1, 2), \tag{82}$$

and a_1, a_2, b_1 and b_2 are constants. Here, μ_1 is larger than μ_2, and they satisfy the relations

$$\mu_1^2 + \mu_2^2 = \frac{\tilde{R}_1}{2\pi^2}, \tag{83}$$

$$\mu_1 \mu_2 = 4\sqrt{3}. \tag{84}$$

It is noted that $\tilde{R}_1$ is larger if the difference between μ_1 and μ_2 is larger.

Because of boundary condition (67), the following equations should be satisfied:

$$a_1 \sin(\mu_1 \tilde{y}_b) + a_2 \sin(\mu_2 \tilde{y}_b) = 0, \tag{85}$$

$$b_1 \cos(\mu_1 \tilde{y}_b) + b_2 \cos(\mu_2 \tilde{y}_b) = 0. \tag{86}$$

Moreover, from boundary condition (79), we obtain

$$a_1 \mu_2 \cos(\mu_1 \tilde{y}_b) + a_2 \mu_1 \cos(\mu_2 \tilde{y}_b) = 0, \tag{87}$$

$$b_1 \mu_2 \sin(\mu_1 \tilde{y}_b) + b_2 \mu_1 \sin(\mu_2 \tilde{y}_b) = 0, \tag{88}$$

by using equation (83). The condition for the existence of non-zero a_1 and a_2 satisfying equations (85) and (87) is written as

$$\mu_1 \tan(\mu_1 \tilde{y}_b) = \mu_2 \tan(\mu_2 \tilde{y}_b), \tag{89}$$

whereas the condition for the existence of non-zero b_1 and b_2 satisfying equations (86) and (88) is written as

$$\mu_1 \cot(\mu_1 \tilde{y}_b) = \mu_2 \cot(\mu_2 \tilde{y}_b). \tag{90}$$

If a value of $\tilde{y}_b$ is given, μ_1 and μ_2 of odd $\tilde{Y}_w$ expressed as equation (80) are obtained as the solution to equations (84) and (89), whereas μ_1 and μ_2 of even $\tilde{Y}_w$ given by equation (81) are the solution to equations (84) and (90). Here, although there are infinite number of pairs of μ_1 and μ_2 satisfying equations (84) and (89) or (90), we choose the pair of smallest difference so that $\tilde{R}_1$ determined from equation (83) is the smallest. For fixed A_y, the values of μ_1, μ_2 and $\tilde{R}_1$ for any A_x are numerically obtained through the above procedure by using $\tilde{y}_b = A_y/(2\sqrt{A_x})$. The dependence of $\tilde{R}_1$ on A_x for $A_y = 1$ is shown in figure 15(a). Both for odd and even $\tilde{Y}_w$, $\tilde{R}_1$ decreases with the decrease in A_x, and tends to $\tilde{R}_{1\infty}$. We also observe a few intersections of the $\tilde{R}_1$ curves for even and odd $\tilde{Y}_w$, corresponding to the change of most unstable mode between $\hat{\theta}(e, e, e)$ and $\hat{\theta}(e, o, e)$ modes. The R_c for $\hat{\theta}(e, e, e)$ and $\hat{\theta}(e, o, e)$ modes in the asymptotic analysis are obtained by substituting $\tilde{R}_0 = \pi^4$ and $\tilde{R}_1$ for even and odd $\tilde{Y}_w$ into equation (43). The $\tilde{R}_c \equiv R_c A_x^4/\pi^4$ based on these R_c, shown in figure 15(b) as thin and thick

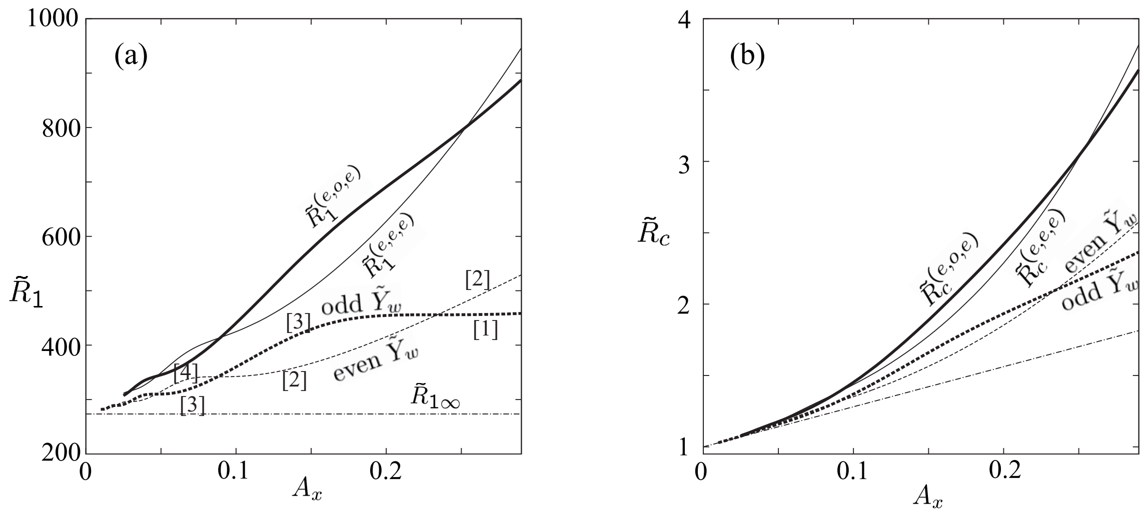

Figure 15. (a): Thick and thin broken lines denote the $\tilde{R}_1$ for odd and even $\tilde{Y}_w$, respectively. $\tilde{R}_{1\infty}$ is expressed by a dotted-broken line. Numbers in [ ] denote the number of convection rolls, N_v. $\tilde{R}_1^{(e,o,e)}$ and $\tilde{R}_1^{(e,e,e)}$ denoted by thick and thin solid lines are defined by equation (99). $A_y = 1$. (b): Thick and thin broken lines denote the $\tilde{R}_c \equiv R_c A_x^4/\pi^4$ computed from equation (101) with the $\tilde{R}_1$ for odd and even $\tilde{Y}_w$, respectively, whereas dotted-broken line denotes the $\tilde{R}_c$ obtained by using $\tilde{R}_1 = \tilde{R}_{1\infty}$ in equation (101). $\tilde{R}_c^{(e,o,e)}$ and $\tilde{R}_c^{(e,e,e)}$ denoted by thick and thin solid lines are defined by equation (100). $A_y = 1$.

broken lines, decreases to 1 as A_x decreases to 0 both for even and odd $\tilde{Y}_w$, and is well approximated by the $\tilde{R}_c$ computed from $\tilde{R}_0 = \pi^4$ and $\tilde{R}_1 = \tilde{R}_{1\infty}$ expressed by a straight dotted-broken line for small A_x.

The A_x's at the intersections of $\tilde{R}_1$ curves for odd and even $\tilde{Y}_w$ can be obtained in the asymptotic analysis. That is, if $\tilde{R}_1$'s for odd and even $\tilde{Y}_w$ are the same, the μ_1 and μ_2 for odd $\tilde{Y}_w$ agree with those for even $\tilde{Y}_w$. Therefore, these μ_1 and μ_2 are required to satisfy equations (89) and (90) simultaneously. The series of μ_1 and μ_2 satisfying these equations are written as

$$\mu_1 = \frac{(N_b+1)\pi}{\tilde{y}_b}, \quad \mu_2 = \frac{N_b\pi}{\tilde{y}_b} \quad (N_b = 1, 2, \ldots), \tag{91}$$

or

$$\mu_1 = \frac{(N_b+\frac{1}{2})\pi}{\tilde{y}_b}, \quad \mu_2 = \frac{(N_b-\frac{1}{2})\pi}{\tilde{y}_b} \quad (N_b = 1, 2, \ldots). \tag{92}$$

When equation (91) is satisfied, we obtain

$$\tilde{y}_b = \tilde{y}_{b(eo)}^{(N_b)}, \quad \text{where} \quad \tilde{y}_{b(eo)}^{(N_b)} \equiv \sqrt{\frac{N_b(N_b+1)}{4\sqrt{3}}}\pi \quad (N_b = 1, 2, \ldots), \tag{93}$$

$$\tilde{R}_1 = \tilde{R}_{1(eo)}^{(N_b)}, \quad \text{where} \ \tilde{R}_{1(eo)}^{(N_b)} \equiv \tilde{R}_{1\infty}\left[1 + \frac{1}{2N_b(N_b+1)}\right] \quad (N_b = 1, 2, \ldots), \tag{94}$$

from equations (83) and (84), whereas

$$\tilde{y}_b = \tilde{y}_{b(oe)}^{(N_b)}, \quad \text{where} \quad \tilde{y}_{b(oe)}^{(N_b)} \equiv \sqrt{\frac{N_b^2 - \frac{1}{4}}{4\sqrt{3}}}\pi \quad (N_b = 1, 2, \ldots), \tag{95}$$

$$\tilde{R}_1 = \tilde{R}_{1(oe)}^{(N_b)}, \quad \text{where} \quad \tilde{R}_{1(oe)}^{(N_b)} \equiv \tilde{R}_{1\infty}\left[1 + \frac{1}{2(N_b^2 - \frac{1}{4})}\right] \quad (N_b = 1, 2, \ldots), \tag{96}$$

are obtained from the same equations if equation (92) is satisfied. Both of the above two expressions of $\tilde{R}_1$ can be rewritten as

$$\tilde{R}_1 = \tilde{R}_{1\infty}\left(1 + \frac{\pi^2}{8\sqrt{3}\tilde{y}_b^2}\right), \tag{97}$$

for any N_b.

The $\tilde{y}_b$'s defined by equations (93) or (95), which corresponds to the intersections of $\tilde{R}_1$ curves for odd and even $\tilde{Y}_w$, increase roughly proportionally with N_b for large N_b. The $\tilde{R}_1$'s at these intersections decrease with the increase in $\tilde{y}_b$ or N_b, and tend to $\tilde{R}_{1\infty}$ as $\tilde{y}_b$ (or N_b) $\to \infty$, as found from equations (94), (96) and (97). It is also found that the relation $\tilde{y}_{b(oe)}^{(N_b)} < \tilde{y}_{b(eo)}^{(N_b)} < \tilde{y}_{b(oe)}^{(N_b+1)}$ holds for any positive integer N_b. The values of $\tilde{y}_b$ and $\tilde{R}_1$ given by equations (93)–(96) for $N_b = 1, 2$ and 3 are shown in Table 3 in ascending order of $\tilde{y}_b$. The values of A_x based on the above $\tilde{y}_b$ for $A_y = 1$ are also shown in this table to compare with the numerical results.

Table 3. Values of $\tilde{y}_b$ and $\tilde{R}_1$ given by equations (93)–(96). Values of A_x based on this $\tilde{y}_b$ and numerically computed A_x where the most unstable mode changes for $A_y = 1$.

(eo) or (oe)	N_b	$\tilde{y}_b$	$\tilde{R}_1$	A_x based on $\tilde{y}_b$ for $A_y = 1$	A_x where the most unstable mode changes for $A_y = 1$	change of N_v of most unstable mode with the increase in $\tilde{y}_b$
(oe)	1	1.0336	455.86	0.2340	0.2533	$1 \to 2$
(eo)	1	1.6879	341.89	0.0877	0.0898	$2 \to 3$
(oe)	2	2.3113	309.98	0.0468	0.0474	$3 \to 4$
(eo)	2	2.9236	296.31	0.0292	0.0295	$4 \to 5$
(oe)	3	3.5306	289.14	0.0201	0.0202	$5 \to 6$
(eo)	3	4.1346	284.91	0.0146	0.0147	$6 \to 7$

The number of convection rolls, N_v, agrees with the number of zeros of the profile of y-dependence of w in the region of $-A_y/2 < y < A_y/2$, as found from the comparison of figures 5 and 9(a) and (b). The y-dependence of normalized w is determined by $\tilde{Y}_w$ in the asymptotic analysis. For each $\tilde{y}_b$, because the ratios of coefficients, a_2/a_1 and b_2/b_1, in equations (80) and (81) are determined from equations (85) and (86) (or equations (87) and (88)), the profiles of even and odd $\tilde{Y}_w$ are obtained. On the basis of the number of zeros of these $\tilde{Y}_w$, we obtain the results that at $\tilde{y}_b = \tilde{y}_{b(eo)}^{(N_b)}$, the change of most unstable mode between the even $\tilde{Y}_w$ with $N_v = 2N_b$ and the odd $\tilde{Y}_w$ with $N_v = 2N_b + 1$ occurs, and that at $\tilde{y}_b = \tilde{y}_{b(oe)}^{(N_b)}$, the change between the odd $\tilde{Y}_w$ with $N_v = 2N_b - 1$ and the even $\tilde{Y}_w$ with $N_v = 2N_b$ occurs. Therefore, as $\tilde{y}_b$ increases, the N_v of most unstable mode increases by 1 at the above $\tilde{y}_b$'s, as shown in Table 3. This behavior corresponds to the increase in the N_v one by one with the decrease in A_x for fixed A_y, as shown in figures 3, 4(a) and 15(a). For large N_b, the N_v is approximated by $2N_b$, and both $\tilde{y}_{b(eo)}^{(N_b)}$ and $\tilde{y}_{b(oe)}^{(N_b)}$ are approximated by $\pi N_b/(2\cdot 3^{\frac{1}{4}})$. Therefore, we obtain the following approximate expression of N_v:

$$N_v = \frac{2\cdot 3^{\frac{1}{4}} A_y}{\pi\sqrt{A_x}}. \tag{98}$$

The results of asymptotic analysis obtained in this subsection agree well with the numerical results for small A_x shown in section 5.1. That is, in the asymptotic analysis, the boundary lines in the (A_x, A_y) plane across which the most unstable mode changes are determined from $\tilde{y}_b = \tilde{y}_{b(eo)}^{(N_b)}$ and $\tilde{y}_b = \tilde{y}_{b(oe)}^{(N_b)}$. These boundary lines denoted by broken lines in figure 3 agree well with the numerical boundary lines for small A_x, although their difference is not small for A_x around 1. Moreover, for $A_y = 1$, quite good agreement between analytical and numerical A_x's where the most unstable mode changes is observed for small A_x, as found from Table 3. The relation between A_x and N_v given by equation (98) is shown in figure 6 by broken lines for $A_y = 1$ and 6. We find that the dependence of N_v on A_x in the numerical computation for small A_x is consistent with these lines. It is also found that the one-by-one increase in the N_v of most unstable mode with the decrease in A_x for fixed A_y in the numerical computations is perfectly explained by the asymptotic analysis.

The values of $\tilde{R}_1^{(e,e,e)}$ and $\tilde{R}_1^{(e,o,e)}$ defined by

$$\tilde{R}_1^{(e,s_y,e)} \equiv \frac{A_x^4 R_c^{(e,s_y,e)} - \pi^4}{A_x} \quad (s_y = e \text{ or } o), \tag{99}$$

obtained in the numerical computation, correspond to the $\tilde{R}_1$ in the asymptotic analysis for even and odd $\tilde{Y}_w$, respectively. The dependence of $\tilde{R}_1^{(e,o,e)}$ and $\tilde{R}_1^{(e,e,e)}$ on A_x for $A_y = 1$ is expressed by thick and thin solid lines in figure 15(a), respectively. Although they are larger than the $\tilde{R}_1$ for odd and even $\tilde{Y}_w$, their deviation from this $\tilde{R}_1$ decreases as A_x decreases, and they tend to $\tilde{R}_{1\infty}$ as $A_x \to 0$. The dependence of $\tilde{R}_c^{(e,e,e)}$ and $\tilde{R}_c^{(e,o,e)}$ defined by

$$\tilde{R}_c^{(e,s_y,e)} \equiv R_c^{(e,s_y,e)} A_x^4/\pi^4 \quad (s_y = e \text{ or } o), \tag{100}$$

obtained in the numerical computation, on A_x for $A_y = 1$ is expressed by solid lines in figure 15(b). The dependence of the analytical result of $\tilde{R}_c$ defined by

$$\tilde{R}_c \equiv 1 + \frac{A_x \tilde{R}_1}{\pi^4}, \tag{101}$$

with the $\tilde{R}_1$ for even and odd $\tilde{Y}_w$ on A_x for $A_y = 1$ is shown in figure 15(b) as thin and thick broken lines, respectively, whereas the dependence of the $\tilde{R}_c$ with $\tilde{R}_1 = \tilde{R}_{1\infty}$ on A_x is expressed as a dotted-broken line. Both $\tilde{R}_c^{(e,e,e)}$ and $\tilde{R}_c^{(e,o,e)}$ are tangent to the line of the $\tilde{R}_c$ with $\tilde{R}_1 = \tilde{R}_{1\infty}$ in the limit of $A_x \to 0$, and are well approximated by the $\tilde{R}_c$ with the $\tilde{R}_1$ for even and odd $\tilde{Y}_w$ for small A_x.

The numerical profiles of normalized u, v and w of most unstable mode shown in figures 7–9 also agree well with the profiles obtained in the asymptotic analysis outside the wall layers. That is, the z-dependence of normalized w shown in figure 7(a) is well approximated by the analytical profile of $\tilde{Z}_w = \cos(\pi z)$ of equation (75), denoted by $\circ$, except for a slight discrepancy near $z = \pm 0.5$. The z-dependences of normalized u and v shown in figures 7(b) and (c) are also close to the analytical profile of $\sqrt{2}\sin(\pi z)$, denoted by $\square$ and $+$, derived from equations (63), (64) and (75) except in the wall layers. The x-dependences of normalized u, v and w outside the wall layers shown in figure 8 are well approximated by the analytical profiles obtained by normalizing the $\tilde{u}_0, \tilde{v}_0$ and $\tilde{w}_0$ given by equations (63), (64) and (59), expressed by $\square, +$ and $\circ$, respectively. The y-dependences of normalized u and w shown in figures 9(a)–(d) also agree well with the normalized profiles of $\tilde{Y}_w$ expressing the y-dependence of $\tilde{u}_0$ and $\tilde{w}_0$ in equations (63) and (59), denoted by $\square$ and $\circ$, both for $\hat{\theta}(e,e,e)$ and $\hat{\theta}(e,o,e)$ modes. Moreover, the y-dependences of normalized v shown in figures 9(e) and (f) are well approximated by the normalized y-dependences of $\tilde{v}_0$, denoted by $+$, obtained by substituting even and odd $\tilde{Y}_w$ into equation (64), respectively.

6.2. The case of $A_x = A_y = A \ll 1$

Most of the numerical results for $A \ll 1$ shown in section 5.2 also can be explained by using an asymptotic analysis under a few assumptions based on the numerical results. That is, in consideration of the results shown in figures 11 and 14, we assume that $u, v, w, \hat{\theta}$ and R_c are expressed as

$$\begin{cases} u = A(\hat{u}_0 + A^2\hat{u}_1),\ \ v = A(\hat{v}_0 + A^2\hat{v}_1),\ \ w = \hat{w}_0 + A^2\hat{w}_1, \\ \hat{\theta} = A^2(\hat{\theta}_0 + A^2\hat{\theta}_1),\ \ R_c = A^{-4}(\hat{R}_0 + A^2\hat{R}_1), \end{cases} \tag{102}$$

for small A, where functions $\hat{u}_0, \hat{v}_0, \hat{w}_0, \hat{\theta}_0, \hat{u}_1, \hat{v}_1, \hat{w}_1$ and $\hat{\theta}_1$ are independent of A, and $\hat{R}_0$ and $\hat{R}_1$ are constants independent of A. It is also assumed that these functions depend on

$$\hat{x} \equiv \frac{1}{A}x, \quad \hat{y} \equiv \frac{1}{A}y,$$

and z, because the representative horizontal scale of $\boldsymbol{\hat{u}}$ and $\hat{\theta}$ is expected to be of O(A).

If we substitute equation (102) into equation (41), we obtain

$$\hat{w}_0 = -\hat{\Delta}_H\hat{\theta}_0, \tag{103}$$

at the leading order of A, and

$$\hat{w}_1 = -\hat{\Delta}_H\hat{\theta}_1 - \frac{\partial^2\hat{\theta}_0}{\partial z^2}, \tag{104}$$

at the next order of A, where

$$\hat{\Delta}_H \equiv \frac{\partial^2}{\partial \hat{x}^2} + \frac{\partial^2}{\partial \hat{y}^2}.$$

Substituting equation (102) into equations (39) and (40), we obtain

$$\frac{\partial}{\partial \hat{x}} \hat{\Delta}_H \hat{w}_0 + \hat{R}_0 \frac{\partial \hat{\theta}_0}{\partial \hat{x}} = 0, \tag{105}$$

$$\frac{\partial}{\partial \hat{y}} \hat{\Delta}_H \hat{w}_0 + \hat{R}_0 \frac{\partial \hat{\theta}_0}{\partial \hat{y}} = 0, \tag{106}$$

at the leading order, and

$$-\frac{\partial}{\partial z} \hat{\Delta}_H \hat{u}_0 + \frac{\partial}{\partial \hat{x}} \left(\hat{\Delta}_H \hat{w}_1 + \frac{\partial^2 \hat{w}_0}{\partial z^2} \right) + \hat{R}_1 \frac{\partial \hat{\theta}_0}{\partial \hat{x}} + \hat{R}_0 \frac{\partial \hat{\theta}_1}{\partial \hat{x}} = 0, \tag{107}$$

$$-\frac{\partial}{\partial z} \hat{\Delta}_H \hat{v}_0 + \frac{\partial}{\partial \hat{y}} \left(\hat{\Delta}_H \hat{w}_1 + \frac{\partial^2 \hat{w}_0}{\partial z^2} \right) + \hat{R}_1 \frac{\partial \hat{\theta}_0}{\partial \hat{y}} + \hat{R}_0 \frac{\partial \hat{\theta}_1}{\partial \hat{y}} = 0, \tag{108}$$

at the next order. Substitution of equation (102) into equations (37) and (38) yields

$$\frac{\partial \hat{u}_0}{\partial \hat{x}} + \frac{\partial \hat{v}_0}{\partial \hat{y}} + \frac{\partial \hat{w}_0}{\partial z} = 0, \tag{109}$$

$$\frac{\partial}{\partial \hat{y}} \hat{\Delta}_H \hat{u}_0 - \frac{\partial}{\partial \hat{x}} \hat{\Delta}_H \hat{v}_0 = 0, \tag{110}$$

at the leading order.

From equations (103), (105) and (106), we obtain the following equation for $\hat{w}_0$:

$$\hat{\Delta}_H^2 \hat{w}_0 = \hat{R}_0 \hat{w}_0. \tag{111}$$

Here, the numerical results shown in figure 13 suggest that for small A, w can be expressed as a product of a function of $\hat{x}$, a function of $\hat{y}$ and a function of z except in the wall layers. Therefore, we assume that $\hat{w}_0$ is expressed as

$$\hat{w}_0 = \hat{X}_w(\hat{x}) \hat{Y}_w(\hat{y}) \hat{Z}_w(z), \tag{112}$$

where $\hat{X}_w, \hat{Y}_w$ and $\hat{Z}_w$ are functions of $\hat{x}$, $\hat{y}$ and z, respectively. From the equation obtained by substituting equation (112) into equation (111) and the boundary condition of $\hat{w}_0 = 0$ on the walls, we find that $\hat{X}_w$ and $\hat{Y}_w$ should satisfy

$$\frac{d^2 \hat{X}_w}{d\hat{x}^2} = c_1 \hat{X}_w, \qquad \frac{d^2 \hat{Y}_w}{d\hat{y}^2} = c_2 \hat{Y}_w, \tag{113}$$

$$\hat{X}_w = 0 \quad \text{at} \quad \hat{x} = \pm\frac{1}{2}, \qquad \hat{Y}_w = 0 \quad \text{at} \quad \hat{y} = \pm\frac{1}{2}, \tag{114}$$

where c_1 and c_2 are constants. Moreover, we obtain the relation

$$\hat{R}_0 = (c_1 + c_2)^2, \tag{115}$$

from equations (111)–(113). The even function $\hat{X}_w$ and odd function $\hat{Y}_w$ that satisfy equation (113) and boundary condition (114) and that yield the smallest $\hat{R}_0$ are written as

$$\hat{X}_w = \cos(\pi\hat{x}), \ \hat{Y}_w = \sin(2\pi\hat{y}), \tag{116}$$

which give $c_1 = -\pi^2$ and $c_2 = -4\pi^2$. Therefore, we obtain

$$\hat{w}_0 = \cos(\pi\hat{x})\sin(2\pi\hat{y})\hat{Z}_w(z), \ \hat{R}_0 = 25\pi^4. \tag{117}$$

Here it is noted that although the solution of different symmetry expressed as $\hat{w}_0 = \cos(\pi\hat{x})\cos(\pi\hat{y})\hat{Z}_w(z)$ yields $\hat{R}_0$ smaller than $25\pi^4$, this solution is not valid because it gives non-zero vertical flux through any horizontal section of the cavity. From equations (103) and (117) and boundary conditions on the walls, we find that $\hat{\theta}_0$ is related to $\hat{w}_0$ as

$$\hat{\theta}_0 = \frac{1}{5\pi^2}\hat{w}_0. \tag{118}$$

The numerical results shown in figure 13 suggest that u and v for small A can be expressed as products of a function of z that is common to u and v and functions of $\hat{x}$ and $\hat{y}$ except in the wall layers. Therefore, we assume that $\hat{u}_0$ and $\hat{v}_0$ are expressed as

$$\hat{u}_0 = P_u(\hat{x},\hat{y})Z_h(z), \ \hat{v}_0 = P_v(\hat{x},\hat{y})Z_h(z), \tag{119}$$

outside the wall layers, where P_u and P_v are functions of $\hat{x}$ and $\hat{y}$, and Z_h is a function of z. From equations (109), (110), (117) and (119), we obtain

$$Z_h = \gamma\frac{d\hat{Z}_w}{dz}, \tag{120}$$

$$\hat{\Delta}_H^2 P_u = -\frac{5\pi^3}{\gamma}\sin(\pi\hat{x})\sin(2\pi\hat{y}), \ \hat{\Delta}_H^2 P_v = \frac{10\pi^3}{\gamma}\cos(\pi\hat{x})\cos(2\pi\hat{y}), \tag{121}$$

where γ is a non-zero constant. If we assume that P_u and P_v are expressed as products in which their dependences on $\hat{x}$ and $\hat{y}$ are separated, we cannot find their analytic forms that satisfy equation (121) and boundary conditions on the walls. This result suggests that neither P_u nor P_v can be expressed as such products, and is consistent with the numerical result shown in figure 13.

From equations (103), (104), (107), (108), (117) and (118), we can derive the following equation for $\hat{w}_1$:

$$(\hat{\Delta}_H^2 - \hat{R}_0)\hat{w}_1 = 15\pi^2\frac{\partial^2\hat{w}_0}{\partial z^2} + \hat{R}_1\hat{w}_0. \tag{122}$$

From the solvability condition for inhomogeneous equation (122) having the same homogeneous terms and the same eigenvalue parameter value, the inhomogeneous term of this equation should be 0. Therefore, by using equation (117), we obtain the following equation:

$$15\pi^2\frac{d^2\hat{Z}_w}{dz^2} + \hat{R}_1\hat{Z}_w = 0. \tag{123}$$

The even function $\hat{Z}_w$ that satisfies equation (123) and the boundary condition of $\hat{Z}_w = 0$ at $z = \pm 1/2$ and also gives the smallest $\hat{R}_1$ is written as

$$\hat{Z}_w = \cos(\pi z), \tag{124}$$

for which

$$\hat{R}_1 = 15\pi^4, \tag{125}$$

is derived. Therefore, from equations (102), (117) and (125), we obtain

$$R_c = 25\pi^4 A^{-4}\left(1 + \frac{3}{5}A^2\right). \tag{126}$$

Function Z_h is expressed as

$$Z_h = -\gamma\pi \sin(\pi z), \tag{127}$$

from equations (120) and (124). Therefore, the profile of Z_h that is normalized in the same way as the numerical profiles of z-dependences of normalized u and v is given by

$$Z_h = \sqrt{2}\sin(\pi z). \tag{128}$$

It is noted that this Z_h approaches $\sqrt{2}$ as z tends to $1/2$ and does not satisfy the boundary condition of $Z_h = 0$ at $z = \pm 1/2$.

The above analytical results agree well with the numerical results for $A \ll 1$ outside the wall layers. That is, in figure 11 we find that the numerical value of $R_c A^4/(25\pi^4)$ for small A is well approximated by $1 + 3A^2/5$ obtained from equation (126), denoted by a broken line. The numerical profiles of the z-dependences of normalized u and v agree well with the analytical profiles given by equation (128), denoted by $\circ$ in figure 13(a), except in the wall layer. The numerical profiles of the x-, y- and z-dependences of normalized w shown in figures 13(b), (c) and (a) are also well approximated by the analytical profiles of $\cos(\pi x/A)$, $\sin(2\pi y/A)$ and $\cos(\pi z)$, respectively, denoted by $+$, except in the wall layer. It is noted that in the wall layers the difference between the numerical and analytical profiles of the z-dependences of normalized u and v is large, as found from figure 13(a).

7. Discussion and Conclusions

Onset of thermal convection of a fluid in a rectangular parallelepiped cavity of small aspect ratios is examined both numerically and analytically under the assumption that its all walls are rigid and of perfect thermal conductance exposed to a vertically linear temperature field. Critical Rayleigh number R_c and the steady velocity and temperature fields of most unstable mode are computed by a Galerkin spectral method of high accuracy described in section 3 for aspect ratios A_x and A_y either or both of which are small.

In section 5.1, we find that if A_x is decreased to 0 with A_y being kept constant, R_c increases proportionally to A_x^{-4}, the convection rolls of most unstable mode whose axes are parallel to the shorter side walls become narrower, and their number increases proportionally to $A_x^{-\frac{1}{2}}$. We also observe more frequent changes of the symmetry of most unstable mode for smaller A_x. However, if $A_x = A_y = A$ is decreased to 0, although we again observe the increase in R_c proportional to A^{-4}, we always obtain the flow pattern of most unstable mode composed of a narrow convection roll, as shown in section 5.2. The existence of the thin wall layers near the top and bottom walls within which rapid variations of horizontal velocity components are found is also observed for small A_x or A.

Using the dependences of R_c and the magnitude and length scale of the velocity field of most unstable mode on A_x and A_y in the numerical computations, the expressions of R_c and velocity fields in the limit of $A_x \to 0$ or $A \to 0$ are obtained by an asymptotic analysis in section 6. For example, R_c is approximated by $\pi^4 A_x^{-4}$ and $25\pi^4 A^{-4}$ in the limits of $A_x \to 0$ and $A \to 0$, respectively. Moreover, second-order expressions of R_c are derived both for $A_x \to 0$ and $A \to 0$. The analytical expressions of all components of velocity fields for $A_x \to 0$ and the vertical component of velocity fields for $A \to 0$ are also derived. Moreover, the analytical expressions of boundary lines in the (A_x, A_y) plane across which the most unstable mode changes for small A_x are derived.

The results of the asymptotic analysis obtained in section 6 agree well with the numerical results for small A_x or A. That is, the numerical values of R_c for small A_x or A are well approximated by its analytical expressions. The one-by-one increase in the number of convection rolls of most unstable mode with the decrease in A_x for A_y being kept constant observed in the numerical computations is perfectly explained by the asymptotic analysis. The numerical boundary lines in the (A_x, A_y) plane where the changes of most unstable mode occur for small A_x are close to the boundary lines obtained in the asymptotic analysis. The agreement between the numerical velocity field for small A_x or A and the analytical expressions of velocity field is quite good except in the wall layers.

In his study under the assumption of finite roll, Davis (1967) pointed out that the flow patterns of most unstable mode are composed of a few narrow convection rolls when one of A_x and A_y is much smaller than 1, In the present study, similar results are obtained without this assumption by the numerical method of high accuracy, and the details of flow patterns of most unstable mode for such aspect ratios as well as the analytical explanation of them are reported.

One of the characteristic properties of velocity fields when A_x or A is small is the rapid variations of horizontal velocity components in the wall layers. The existence of the wall layers is shown clearly in the present numerical study of high accuracy. The asymptotic analysis in the present paper yields the velocity profile that cannot satisfy all the boundary conditions on the top and bottom walls. Therefore, these velocity profiles are not valid in the wall layers. Within the wall layers, a scaling of variables different from the one used in the present study would be necessary. The analytical examination of velocity profiles in the wall layers is left for the future study.

In their studies on the onset of thermal convection in an infinite channel of rectangular cross-section surrounded by rigid walls of perfect thermal conductance, Chana and Daniels (1989) numerically obtained the R_c and non-dimensionalized critical wavenumber k_c that determines the width-to-height ratio of the convection rolls of most unstable mode for several aspect ratio A_x of the cross-section. Their results that as A_x decreases to 0, R_c rapidly increases and k_c also increases (that is, the convection rolls become narrower) are consistent with the numerical results of the present study for small A_x with A_y being kept constant. They also performed an asymptotic analysis in the limit of $A_x \to 0$. In this analysis, they adopted the assumptions that are essentially the same as equations (43) and (44), and obtained the asymptotic form of $R_c = A_x^{-4}(\pi^4 + A_x \tilde{R}_{1\infty})$, which is the same as the result of the present study for $\tilde{y}_b \to 0$. Moreover, the expressions of $\tilde{x}$- and z-dependences of $\tilde{u}_0, \tilde{v}_0$ and $\tilde{w}_0$ shown in section 6.1 of the present study were obtained also in their analysis. Therefore, the result of their analysis is consistent with the analytical result of the present study for $\tilde{y}_b \to \infty$.

The results of the asymptotic analysis for $A_x \ll 1$ agree well with the numerical results of R_c and the velocity field of most unstable mode outside the wall layers for small A_x. This agreement suggests that the neglect of the wall layers does not greatly influence the onset of thermal convection for small A_x and that the boundary condition on the top and bottom walls is insignificant for such A_x, which coincides with the assertion of Chana and Daniels (1989) based on their study for both rigid and stress-free top and bottom walls.

It is interesting to examine the effect of imperfection that the cavity is tilted slightly because this effect may cause a remarkable change in the thermal convection of the tall or thin rectangular parallelepiped cavity examined in the present study. The examination of this effect is left for the future study.

References

Catton, I. 1970. Convection in a closed rectangular region: the onset of motion, ASME J. Heat Transfer, pp.186-188.

Chana, M. S. and Daniels, P. G. 1989. Onset of Rayleigh-Bénard convection in a rigid channel, J. Fluid Mech., **199**, pp.257-279.

Daniels, P. G. and Ong, C. F. 1990. Linear stability of convection in a rigid channel uniformly heated from below, Int. J. Heat Mass Transfer, **33**, pp.55-60.

Dauby, P. C. and Lebon, G. 1996. Bénard-Marangoni instability in rigid rectangular containers, J. Fluid Mech., **329**, pp.25-64.

Davies-Jones, R. P. 1970. Thermal convection in an infinite channel with no-slip sidewalls, J. Fluid Mech., **44**, pp.695-704.

Davis, S. H. 1967. Convection in a box: linear theory, J. Fluid Mech., **30**, pp.465-478.

Edwards, B. F. 1988. Crossed rolls at onset of convection in a rigid box, J. Fluid Mech., **191**, pp.583-597.

Fukazawa, Y. and Funakoshi, M. 2015. Onset of thermal convection and its flow patterns in a rectangular cavity, Fluid Dyn. Res., **47**, 065505.

Gelfgat, A. Y. 1999. Different modes of Rayleigh-Bénard instability in two- and three-dimensional rectangular enclosures, J. Comp. Phys., **156**, pp.300-324.

Gershuni, G. Z. and Zhukhovitskii, E. M. 1972. "Convective Stability of Incompressible Fluids," (Nauka, Moscow, English Translation: Keter Publishing House, Jerusalem, 1976) Chapter IV.

Kirchartz, K. R. and Oertel Jr, H. 1988. Three-dimensional thermal cellular convection in rectangular boxes, J. Fluid Mech., **192**, pp.249-286.

Koschmieder, E. L. 1966. On convection on a uniformly heated plane, Beitr. Phys. Atmos., **39**, pp.1-11.

Koschmieder, E. L. 1993. "Bénard Cells and Taylor Vortices," (Cambridge University Press) Section 5.2.

Lappa, M. 2010. "Thermal Convection: Patterns, Evolution and Stability," (John Wiley & Sons) Chapter 4.

Mizushima, J. and Matsuda, O. 1996. (in Japanese) Res. Inst. Appl. Math., Kyoto Univ. Kokyuroku, **970**, pp.1-9.

Mizushima, J. and Matsuda, O. 1997. Onset of 3D thermal convection in a cubic cavity, J. Phys. Soc. Jpn., **66,** pp.2337-2341.

Mizushima, J. and Nakamura, T. 2003. Onset of three-dimensional thermal convection in a rectangular parallelepiped cavity, J. Phys. Soc. Jpn., **72,** pp.197-200.

Puigjaner, D., Herrero, J., Giralt, F. and Simó, C. 2006, Bifurcation analysis of multiple steady flow patterns for Rayleigh-Bénard convection in a cubical cavity at Pr=130, Phys. Rev. E, **73**, 046304.

Puigjaner, D., Herrero, J., Simó, C. and Giralt, F. 2008. Bifurcation analysis of steady Rayleigh-Bénard convection in a cubical cavity with conducting sidewalls, J. Fluid Mech., **598**, pp.393-427.

Sherman, M. and Ostrach, S. 1966. On the principle of exchange of stabilities for the magnetohydrodynamic thermal stability problem in completely confined fluids, J. Fluid Mech., **24**, pp.661-671.

Stork, K. and Müller, U. 1972. Convection in boxes: experiments, J. Fluid Mech., **54**, pp.599-611.